Causes of abundant calcite scaling in geothermal wells in the Bavarian Molasse Basin, Southern Germany

Christoph Wanner[1*], Florian Eichinger[2], Thomas Jahrfeld[3], Larryn W. Diamond[1]

[1]Rock-Water Interaction Group, Institute of Geological Sciences, University of Bern, Baltzerstrasse 3, CH-3012 Bern, Switzerland

[2]Hydroisotop GmbH, Woelkestrasse 9, D-85301 Schweitenkirchen Germany

[3]renerco plan consult, Herzog-Heinrich Strasse 13 D-80336 München, Germany

**corresponding author (wanner@geo.unibe.ch)*

ABSTRACT

The carbonate-dominated Malm aquifer in the Bavarian Molasse Basin in Southern Germany is being widely exploited and explored for geothermal energy. Despite favorable reservoir conditions, the use of geothermal wells for heat and power production is highly challenging. The main difficulty, especially in boreholes >3000 m deep with temperatures >120 °C, is that substantial amounts of calcite scales are hindering the proper operation of the pumps within the wells and of the heat exchangers at the surface. To elucidate the causes of scaling we present an extensive geochemical dataset from the geothermal plant in Kirchstockach. Based on chemical analyses of wellhead water samples, chemical and mineralogical analyses of scales collected along the uppermost 800 m of the production well, and chemical analyses of gas inclusions trapped in calcite-scale crystals, four processes are evaluated that could promote calcite scaling. These are (i) decompression of the produced fluid between the reservoir and the wellhead, (ii)

corrosion of the casing that drives *pH* increase and subsequent calcite solubility decrease, (iii) gas influx from the geothermal reservoir and subsequent stripping of CO_2 from the aqueous fluid, and (iv) boiling within the geothermal well. The effectiveness of the four scenarios was assessed by performing geochemical speciation calculations using the codes TOUGHREACT and CHILLER, which explicitly simulate boiling of aqueous fluids (CHILLER) and take into account the pressure dependence of calcite solubility (TOUGHREACT). The results show that process (i) causes notable calcite supersaturation but cannot act as the sole driver for scaling, whereas (ii) and (iii) are negligible in the present case. In contrast, process (iv) is consistent with all the available observations. That is, scaling is controlled by the exsolution of CO_2 upon boiling at the markedly sub-hydrostatic pressure of 4-6 bar within the production well. This process is confirmed by the visible presence of gas inclusions in the calcite scales at $\leq$ 700 m depth, where the production fluid should nominally have been in the homogeneous liquid state. Whereas minor calcite scaling may have been triggered by fluid decompression within the production well, we conclude that the abundant scaling along the pump casing is due to cavitation induced by operating the pump at high production rates.

1. INTRODUCTION

The precipitation of mineral phases from geothermal fluids (i.e., scales) may pose a serious economic risk to the successful operation of geothermal plants (Thomas and Gudmundsson, 1989). Typical scaling phases include carbonates (Ámannsson, 1989; Arnórsson, 1989; Benoit, 1989; Lindal and Kristmannsdóttir, 1989), amorphous silica and silicates (Gunnarsson and Arnórsson, 2005; Kristmannsdóttir, 1989; Zarrouk et al., 2014), sulphates (Regenspurg et al., 2015) as well as mixed metal oxides and sulfides (Gallup, 1989; Regenspurg

et al., 2015; Wilson et al., 2007), which are often associated with corrosion of parts of the geothermal plant (Honegger et al., 1989; Mundhenk et al., 2013). Scaling phases precipitate when they become supersaturated along the geothermal loop due to gas exsolution or due to a solubility decrease induced by changes in temperature and/or pressure as well as mixing between aqueous solutions with different chemical compositions (Bozau et al., 2015; García et al., 2006; Thomas and Gudmundsson, 1989). Typical problems associated with scaling include clogging of pipes and wells, reduced efficiency of pumps and heat exchangers, reduced reinjection capacity as well as accumulation of hazardous materials (e.g., Pb- and Ra-bearing scales) that require costly disposal (Bozau et al., 2015; García et al., 2006; Scheiber et al., 2013).

Over the past 15 years the Bavarian Molasse Basin in southern Germany has become a veritable hotspot for geothermal power production. Currently 22 geothermal power plants are being operated (Dussel et al., 2016; Lentsch et al., 2015; Mayrhofer et al., 2014). Most of them are located within the greater Munich area. The thermal reservoir for all these plants is the upper Malm aquifer of Upper Jurassic age, which is about 500–600 m thick. This aquifer is dominated by carbonates and has elevated fracture-porosity owing to karstification during the late Cretaceous and early Cenozoic. During the subsequent Alpine orogeny the Malm unit was situated within the evolving northern foreland depression and hence it was progressively buried by the erosional products of the uplifting Alps, creating the Molasse Basin. As a consequence, the upper Malm aquifer now dips southward and reservoir temperatures chiefly depend on the depth of the aquifer at a given location (Fig. 1). A maximum reservoir temperature of about 150 °C is observed to the south where the reservoir depth reaches 4–5 km. The various geothermal plants produce fluids at rates between 40 and 140 L/s. Most of the plants are producing thermal energy. However, SE and S of Munich, where the production temperature is > 120 °C, electrical

69 energy is produced as well. Despite the favorable reservoir conditions, the successful operation
70 of the plants located SE and S of Munich is highly challenging. In about two thirds of the plants
71 producing thermal water with temperatures > 120 °C, substantial calcite scaling is hindering the
72 proper operation of the pumps within the wells and of the heat exchangers at the surface.
73 Worldwide, the formation of calcite scales is mostly attributed to boiling of the geothermal fluid
74 or to CO_2-stripping via degassing of sparingly soluble gases that have a lower solubility than
75 CO_2 (Arnórsson, 1989; Benoit, 1989; Simmons and Christenson, 1994). Thus, the formation of
76 calcite scales in the plants SE and S of Munich is an unexpected phenomenon, because all the
77 plants are being operated at wellhead pressures of 10–20 bar to exceed the experimentally
78 determined degassing pressures, which are in the range of 2–10 bar.
79 This study aims at identifying the main processes controlling calcite scaling in
80 geothermal plants in the area SE of Munich in order to aid in optimizing the operation of these
81 plants. To do so we focus on a particular production period from December 2014 to March 2015
82 at the Kirchstockach plant. This period was chosen because we have good data on the amount of
83 scales formed over this period, on the corresponding production rates and on the evolution of the
84 chemical fluid composition at the wellhead. In addition, we have found liquid and gas inclusions
85 in calcite crystals precipitated from the geothermal fluid during the investigated production
86 period.
87
88 **2. SITE DESCRIPTION**
89 The binary cycle geothermal plant at Kirchstockach is located about 15 km SE of
90 downtown Munich (Fig. 1). It became commercially operational in March 2013 and it consists of
91 a geothermal doublet with one production and one injection well, as well as the power plant at

92 the surface, yielding an installed capacity of 5.5 MW_{el}. Both wells reach depths of about 3900 m
93 (Fig. 2) and were drilled subvertically through the top 2.5 km of sediments. At greater depths the
94 wells deviate horizontally to intersect multiple steeply dipping fracture zones (Cacace et al.,
95 2013; Moeck and Mraz, 2015) (Figs. 1 and 2). As a consequence of the deviations the horizontal
96 distance between the production and injection wells within the reservoir is roughly 2 km,
97 whereas at the surface the two wells are only 20 m from each other. The inner diameter of the
98 production well (inside the casing) is 12.25 inches (31 cm) along the top 2063 m and 8.5 inches
99 (21.6 cm) along the reminder of the well. Along the section within the Malm reservoir no casing
100 is installed (i.e., open hole completion). The plant is being operated using an electrical
101 submersible pumping system with an 8 m long, multi-stage centrifugal pump that is placed in the
102 production well at variable depths between 450 and 900 m. Typical production rates are between
103 80 and 130 L/s at a constant temperature of 135 °C. The reservoir temperature has been
104 measured at 140-141 °C, thus ascent of the fluid through the production well results in only 5-6
105 °C of cooling. Since the start of the commercial power production in March 2013 until the end of
106 our study period on March 15, 2015, the pump had to be replaced 7 times due to technical
107 problems. In most cases, scaling likely caused the failure of various parts of the pumping system,
108 such as the hydraulics of the radial bearings. At the beginning of our study period (December 7,
109 2014) a new riser tube was installed and a pump with a production rate of 80 to 90 L/s was
110 placed at a depth of 800 m. After this period the pump and the overlying pump casing (Fig. 2b)
111 were removed and replaced.
112 Substantial amounts of scales were observed not only in the pump but also along the
113 retrieved pump casing of the production well and in installations of the power plant at the
114 surface, such as within the heat exchanger and at filter cartridges (Fig. 3). Whereas the casing is

115 coated with scales up to ~1 mm thick, veritable “scale rocks” with weights on the order of
116 hundreds of kg are formed over time in tubes of the geothermal plant at the surface (Fig. 3c).
117 These “rocks” are formed by the accumulation of platy scales that had initially formed on the
118 surface of the tubes before being ripped off by turbulence. Such “scale rocks” have to be
119 removed and filter cartridges have to be replaced regularly to ensure the proper operation of the
120 geothermal plant.

121 The Kirchstockach geothermal plant is being operated at 16–18 bar fluid pressure, which
122 is notably higher than the experimentally determined degassing pressure of the wellhead fluid
123 (2–10 bar). Nevertheless, tiny gas bubbles are observed through a small window at the wellhead.
124 Unfortunately, no device is installed to capture this gas phase.

125 The pressure profile along the production well at Kirchstockach is shown in Fig. 2c.
126 Beginning in the reservoir at about 300 bar, the pressure falls linearly with decreasing depth
127 according to a hydrostatic gradient (Fig. 2c). Without pumping, the hydrostatic head on the
128 aquifer stabilizes a water table at ~200 m below the surface. Therefore, during our study period,
129 the pump was placed at 800 m depth to boost the fluid pressure from ~50 bar at its intake (where
130 the exact pressure depends on production rate as well as depth) to ~100 bar at its outlet (kink in
131 Fig. 2c). Above the pump the pressure falls again according to a linear hydrostatic gradient,
132 reaching the wellhead at the target pressure of 16–18 bar. During operation the water table
133 between the riser tube and the well casing (Fig. 2b) lies at 200–250 m depth, depending on the
134 production rate.

135

136

137 **3. METHODS**

138

139 **3.1. Sampling**

140

141 *3.1.1. Scales*

142 The thickness of the scales was measured on each of the 68 casing tubes when the pump
143 casing (Fig. 2b) was taken out of the well on March 15, 2015. Because this casing had been free
144 of scales when it was first installed in the well in December 2014, these measurements pertain to
145 scales precipitated exclusively during the investigated production period (December 7, 2014 to
146 March 15, 2015). Prior to its installation in the well, about 45% of the length of casing had been
147 coated with a thin plastic film to protect it from corrosion and to test the effects of corrosion on
148 scaling. After measuring their thicknesses, roughly 50 g of scales per tube was sampled for
149 analysis. In addition, samples of scales were retrieved from the intake of the pump and from the
150 first stage of the pumping system.

151

152 *3.1.2. Wellhead samples*

153 The produced thermal water was regularly sampled at the wellhead. To do so, the thermal
154 water was cooled down to < 40 °C under operational pressure (16–18 bar) in a specially designed
155 device employing air cooling at a low water flow rate of ~10 mL/s. Subsequently the thermal
156 water was drained under atmospheric pressure to take samples for chemical and in-situ
157 physicochemical parameters. The parameters *pH*, electrical conductivity and redox potential
158 were determined on-site using WTW probes. Alkalinity was determined by titration also on-site.
159 Additionally, thermal water was drained into stainless steel pressure vessels under in-situ
160 pressures and temperatures. These samples were then quantitatively degassed in a closed

161 atmosphere in the laboratory. The degassing pressure was experimentally determined by slowly
162 releasing pressure under in-situ temperature and observing the formation of bubbles via a
163 specially designed viewing system.
164
165 **3.2. Analyses of scales and wellhead fluid samples**
166
167 *3.2.1. Mineralogical and chemical analyses of scales*
168 The mineralogical composition of the scales was determined at the University of Bern on
169 10 of the 68 samples originating from the pump casing overlying the pump (Fig. 2) and on the
170 two samples collected from the pumping system. The main minerals were identified by X-ray
171 powder diffraction (XRD) using a Panalytical X'Pert Pro diffractometer with Cu-Kα radiation
172 (λ=1.54598 Å). Powders were prepared by milling the samples in an agate mortar. To identify
173 accessory minerals, the carbonate fraction of the powders was first removed by dissolution in a
174 few mL of a 2N HCl solution. The remaining sample was then suspended in ethanol and loaded
175 onto silica plates. Following evaporation of the ethanol the XRD analyses were repeated.
176 Minerals were identified from the diffractograms using the Panalytical software "High Score
177 Plus".
178 Elemental analyses were performed at Hydroisotop GmbH on the 10 scale samples for
179 which the mineralogical composition had been determined. The samples were digested in aqua
180 regia (HNO_3 + 3HCl) at 60 °C prior to measuring Na^+, K^+, Mg^{2+}, Ca^{2+} and SO_4^{2+} by ion
181 chromatography using a coupled DIONEX ICS-1500 system. Total dissolved iron was
182 determined using a WTW MultiLab P5 photometer, while the Cu concentration was measured by
183 ICP-MS using a Perkin Elmer Elan 6000 system. The CO_3^{2-} concentration was calculated

184 assuming that Ca^{2+} and Mg^{2+} are exclusively derived from dissolved carbonate minerals ($CaCO_3$
185 and $MgCO_3$ components). The analytical uncertainty is ±5%.
186
187 *3.2.2. Analyses of wellhead fluid samples*
188 The chemical composition of wellhead waters was determined at Hydroisotop GmbH.
189 Concentrations of major cations and anions were measured by ion chromatography (IC) using a
190 coupled DIONEX ICS-1500 system. Based on the observation that HCO_3^- is by far the dominant
191 base in our wellhead samples, its concentration was determined by alkalinity titration performed
192 on-site during sample collection, whereas the concentration of $CO_{2(aq)}$ and other dissolved gases
193 was obtained by quantitative degassing (see below) followed by gas chromatography using a
194 Shimadzu GC-17A WLD/FID system. The analytical uncertainty is ±5%. Total sulfide
195 concentrations were determined by zinc-acetate precipitation followed by ICP-MS analysis.
196
197 *3.2.3. Analyses of fluid inclusions in calcite*
198 Platy calcite scales ~1 mm thick were embedded in epoxy resin and then cut parallel to
199 the growth direction of the calcite crystals (i.e. perpendicular to the well casing). The resulting
200 ~1 mm wide strips of parallel calcite crystals were then polished on both sides to produce
201 transparent microscope sections ~100 μm thick. Petrographic examination of their fluid
202 inclusions was performed using an Olympus BX51 polarizing microscope. Observations were
203 made in normal transmitted light and in UV epi-illumination, which allows identification of
204 fluorescent hydrocarbons.
205
206 *Microthermometry*

Heating experiments were performed on inclusions consisting of liquid + gas bubbles to determine their homogenization temperature (T_h **)**, i.e. the equilibrium temperature at which they transform to a homogeneous (single-phase) liquid state. The measurements were carried out at the University of Bern using a Linkam MSD-600 heating-cooling stage mounted on an Olympus BX51 microscope. The inclusions were viewed during measurements through an Olympus 100x/0.80 LM PlanFI objective lens. The stage was calibrated against the temperature of phase transitions in synthetic fluid inclusions, such that T_h values reported herein are accurate to within ±0.5 °C. The inclusions were photographed before and after heating to check their phase proportions for signs of possible stretching. Replicate measurements were also performed on the same inclusions as a further check on stretching.

Liberation and analysis of gas inclusions

About 7–13 g of scales were crushed in an evacuated piston-cylinder device to liberate gases trapped in fluid inclusions (Eichinger et al., 2010; Hämmerli, 2009; Dublyansky, 2012). Before crushing, the sample chamber was evacuated, flushed twice with He to avoid any air contamination and filled with He to around 400 mbar. During crushing the equipment was heated to 150 °C to avoid gas sorption on the freshly crushed mineral surfaces. After crushing, the device was directly fitted to a gas chromatograph and the pressure and concentrations of the main inorganic gas species (CO_2, N_2, Ar, O_2) and hydrocarbons were measured by GC-WLD and GC-FID (Shimadzu GC-17A), respectively. The volume of the extracted gas species per gram of sample were calculated with respect to the weight of the sample, the gas pressure, the total volume of the piston-cylinder device, and the temperature. Air contamination was quantified by the oxygen concentration and measured gas concentrations were corrected accordingly.

230

231 **3.3. Geochemical modeling**

232

233 *3.3.1. Aqueous speciation calculations*

234 Aqueous speciation calculations were performed using the software TOUGHREACT V3
235 (Xu et al., 2014) to compute the saturation state of calcite and dolomite in wellhead water
236 samples. TOUGHREACT is a modeling code that allows simulation of fully coupled multi-phase
237 and multi-dimensional reactive transport as well as zero-dimensional speciation calculations. Its
238 capabilities have been recently tested in an extended benchmark study (Steefel et al., 2015 and
239 references therein). For this study, aqueous speciation was calculated using the temperature-
240 dependent thermodynamic data in the Soltherm.H06 database (Reed and Palandri, 2006). In
241 addition to taking into account temperature effects on mineral solubilities, TOUGHREACT
242 considers change in equilibrium constants of geochemical reactions as a function of pressure via
243 the relation:

244

245 $$Log(K)_{T,P} = Log(K)_{T,P_0} - \Delta V \cdot \frac{P - P_0}{2.303 \cdot R \cdot T} \quad (1)$$

246

247 where $Log(K)_{T,P}$ and $Log(K)_{T,P0}$ refer to the decadic logarithms of the equilibrium constant K for
248 a given reaction at temperature T (K) and at the pressure P (bar) of reaction and at the reference
249 pressure P_0 (vapor-saturation pressure of pure water at T); R denotes the gas constant (83.14 bar
250 $cm^3\ mol^{-1}\ K^{-1}$); ΔV (cm^3/mol) is the temperature-dependent volume change associated with the
251 given reaction (average ΔV over the pressure interval P_0 to P), which is computed from
252 regression coefficients a_P to e_P:

253

254 $$\Delta V = a_P + b_P \cdot T + c_P \cdot T^2 + d_P / T + e_P / T^2 \quad (2)$$

255

256 Values of Log(K) and ΔV coefficients for reactions relevant to the chemical system of interest
257 are listed in the supporting information. Figure 4 illustrates the effects of pressure and
258 temperature on calcite solubility.

259 Owing to the temperature- and *pH*-dependent speciation of dissolved carbon (HCO_3^- + H^+
260 = $CO_{2(aq)}$ + H_2O), *pH* values and HCO_3^- concentrations vary between sampling at the wellhead
261 (135 °C) and measurements performed on-site (20 °C). For the chemical composition of our
262 wellhead samples both carbon species are relevant, which means that *pH* changes on the order of
263 the measurement uncertainty (±0.1) significantly affect the relative concentrations of $CO_{2(aq)}$ and
264 HCO_3^-. Consequently, on-site *pH* measurements (Table 2) were not used to reconstruct the
265 speciation of the wellhead fluid. Instead, to compute saturation states of calcite and dolomite at
266 the wellhead accurately, the *pH* value and the HCO_3^- and $CO_{2(aq)}$ concentrations were
267 simultaneously reconstructed by speciation calculations performed at wellhead conditions (135
268 °C, 18 bar). To do so, dissolved inorganic carbon (DIC) concentrations were fixed to the sum of
269 $CO_{2(aq)}$ and HCO_3^- concentrations obtained from the concentration measurements of dissolved
270 gases and from the on-site alkalinity titration, respectively, while applying a charge-balance
271 constraint on *pH*. As HCO_3^- is the dominant anion, charge balance was effectively obtained by
272 varying the HCO_3^- concentrations as a function of *pH*.

273

274 *3.3.2. Boiling calculations*

Geochemical effects of degassing possibly occurring within the geothermal loop were assessed by performing boiling calculations using the computer code CHILLER (Reed and Spycher, 2006). In addition to the cited CHILLER manual, details of the numerical approach can be found in Reed (1997; 1998). Unlike TOUGHREACT, CHILLER allows computation of the equilibrium distribution of chemical species between aqueous, gas and mineral phases rather than just between aqueous and solid phases. Similarly to speciation calculations using TOUGHREACT, it calculates aqueous activity coefficients using the extended Debye–Hückel approach (Helgeson et al., 1981), it uses gas fugacities as discussed by Spycher and Reed (1988) and it employs the same thermodynamic database (i.e., Soltherm.H06).

4. RESULTS

4.1. Scale samples

The thickness of scalings precipitated along the pump casing during the 99-day operational period varies from 0.3 to 1.1 mm (Fig. 5). In general, the thickness is slightly lower along the sections of casing coated by plastic. The outer surfaces of the platy scales (i.e. the surfaces originally in contact with the thermal water) are rough, being made up of the euhedral terminations of tiny calcite crystals (~150 μm diam.). The inner surfaces of platy scales originally in direct contact with the plastic coating of the casing are very smooth, white and non-magnetic, whereas those originally in contact with the uncoated casing tubes are rough, dark grey and magnetic. The thickness of scalings precipitated at the intake of the pump and on the impeller of the first stage of the pump is also on the order of 1 mm.

297 The mineralogy is dominated by calcite in all three scaling types (i.e., pump, coated and
298 uncoated casing). However, there are differences with respect to accessory minerals (Table 1). In
299 the pump scales, the Cu-sulfides bornite (Cu_5FeS_4), digenite (Cu_9S_5) and chalcopyrite ($CuFeS_2$)
300 were identified, which presumably are products of partial corrosion of the bronze (i.e, Cu-
301 bearing) radial bearings of the pump. Particularly interesting is the identification of bornite
302 because it can occur as two stable polymorphs: (i) as a low-temperature (<200 °C) orthorhombic
303 phase and (ii) as a high-temperature (>265 °C) cubic phase (Grguric et al., 1998). In our case, the
304 structure of the identified bornite is clearly orthorhombic (see diffractograms provided in the
305 supporting information), although the presence of some of the cubic polymorph cannot be
306 excluded because the diffraction planes of the cubic phase are also present in the structure of the
307 orthorhombic polymorph. In the scales precipitated along the uncoated tubes, the Fe sulfides
308 pyrite (FeS_2) and pyrrhotite (FeS) as well as the iron oxide magnetite (Fe_3O_4) were identified.
309 Judging from the black undersides of the platy scales it is clear that these phases occur only on
310 the surface in contact with the casing. It is thus likely that their formation is due to corrosion of
311 the Fe-bearing casing, which occurs only during the initial stage of scaling. The occurrence of
312 magnetite and pyrrhotite explains the magnetic property of the scales collected from the
313 uncoated casing. In contrast, calcite was the only mineral identified in scales precipitated on the
314 coated casing, demonstrating that the coating successfully protects the casing from corrosion.
315 The mineralogy of the scales is also reflected by their elemental compositions (Table 1).
316 Calcium is the most abundant element in all the scales, in accord with the observed
317 predominance of calcite. The constant Mg/Ca ratio (0.06–0.07 on a molar basis) of the calcite
318 was confirmed by electron microprobe analyses of individual crystals. This demonstrates that the
319 scales are in fact a $CaCO_3$–$MgCO_3$ solid solution (i.e., $Ca_{0.93\text{-}0.94}Mg_{0.06\text{-}0.07}CO_3$) with an ideal

320 $MgCO_3$ activity, $\boldsymbol{a}_{\mathbf{MgCO3}}^{\mathbf{Calcite}}$, of 0.06–0.07, rather than a mixture between calcite and dolomite. No
321 distinct variation in the chemical composition with depth is observed along the 800 m long
322 casing. However, scales from the uncoated casing show a significant Fe and S content reflecting
323 the identified Fe-sulfides and Fe-oxides, whereas Fe and S concentrations are essentially zero in
324 scales from the coated casing. Moreover, scales from the pump show detectable Cu
325 concentrations and the highest of all S concentrations, consistent with the identified Cu-sulphides
326 (bornite, digenite, chalcopyrite).

327 The fact that the sampled scales formed exclusively during the investigated production
328 period (December 2014-March 2015) provides an opportunity to quantify the amount of Ca and
329 CO_2 that precipitated along the riser pipe and to determine the corresponding average calcite
330 deposition rate. This requires determining the total mass of scalings by integrating their thickness
331 over the entire pump casing (Fig. 5) and by taking into account production rates over the
332 investigated operational period (supporting information). Treating the precipitates as pure calcite
333 results in total, time-integrated losses from the production fluid of 0.24 mg/L Ca and 0.27 mg/L
334 CO_2, which yields an average calcite deposition rate of 7.12×10^{-13} mol/L/s.

335

336 **4.2. Wellhead water samples**

337 Concentrations of aqueous species and dissolved gases measured on wellhead samples
338 collected before, during and after the investigated production period are listed in Table 2. Also
339 listed are reconstructed wellhead *pH* values and computed calcite and dolomite saturation indices
340 (*SI*) at wellhead conditions (T = 135 °C, P = 18 bar). Although its effect is only minor (~0.01),
341 the presence of $MgCO_3$ in the calcite solid solution has been taken into account in the listed
342 $SI_{calcite}$ values, calculated according to Reed (1992):

$$SI_{Ca_{0.94}Mg_{0.06}CO_3} = \log(0.094 \cdot 10^{SI_{calcite}} + 0.06 \cdot 10^{SI_{Magnesite}}) \quad (3)$$

The thermal water can be described as a weakly mineralized Na–HCO_3 type, which is typical for thermal water occurring in the Upper Malm aquifer within the Bavarian Molasse Basin. Interestingly, the saturation state of wellhead samples with respect to calcite and dolomite is variable. In most cases, wellhead samples are supersaturated with respect to calcite and dolomite ($SI > 0$). However, three samples were undersaturated with respect to both carbonate phases ($SI < 0$). The saturation indices of calcite and dolomite reflect the variable concentrations of the pertinent dissolved species, as illustrated in Fig. 6a–c by the linear correlations observed between the calcite saturation index and the amount of total dissolved solids (TDS), between the Ca^{2+} concentration and TDS, as well as between the HCO_3^- concentration and TDS. In contrast, very little variation with changing TDS is observed for other major species, such as Na^+ and Cl^- (Fig. 6d). The total dissolved gas content varies between 3.67 and 5.80 mmol/kg (Table 2) and it mainly consists of CO_2, CH_4, and N_2. A significant H_2S concentration was also observed whereas only trace amounts of H_2, ethane, propane and butane were measured.

4.2.1. Reconstruction of reservoir conditions

The fact that calcite and dolomite dissolution rates are rather fast (Palandri and Kharaka, 2004 and references therein) implies that chemical equilibrium is likely to prevail under in-situ reservoir conditions. Therefore, the observation that in most cases wellhead fluid samples are not in equilibrium with respect to calcite and dolomite (Table 2, Fig. 6a) suggests that the wellhead samples do not reflect reservoir conditions. Moreover, the occurrence of calcite scalings along the production well demonstrates that some of the Ca^{2+} and HCO_3^- dissolved under reservoir

366 conditions precipitated from the upflowing thermal water. The formation of calcite scalings is
367 also reflected by the correlations observed between the calcite saturation index and the dissolved
368 calcite species (Figs. 6a-c), suggesting that low concentrations of Ca^{2+} and HCO_3^- at the
369 wellhead are due to greater precipitation of scales at depth.

370 Accordingly, speciation calculations using TOUGHREACT were performed to
371 reconstruct the chemical composition at reservoir conditions (140 °C, 300 bar). To do so the Ca^{2+}
372 concentration was fixed at the maximum value observed at the wellhead (KST-12: 18.9 mg/L,
373 Table 2) because this is likely the sample that experienced the least amount of calcite
374 precipitation within the production well. Moreover, the concentration of total dissolved inorganic
375 carbon (DIC = HCO_3^- + $CO_{2(aq)}$) was numerically increased until calcite and dolomite reached
376 nearly perfect saturation ($SI \approx 0$). The corresponding reservoir *pH* was reconstructed by the total
377 ionisable hydrogen ion balance (Truesdell and Singers, 1974), which means that the total H^+
378 concentration was fixed to the sum of the value calculated for KST-12 and the amount of DIC
379 added to the system. Applying this procedure yielded a reservoir *pH* of 6.44, which is slightly
380 lower than the values reconstructed for the wellhead samples (6.54–6.68), and a reservoir DIC of
381 8 mmol/kg_{H2O} (Table 2), which is 0.5–1.8 mmol/kg_{H2O} higher than DIC concentrations measured
382 in wellhead samples. The increase in DIC is due largely to an increase in $CO_{2(aq)}$ (≈41 mg/kg
383 $CO_{2(aq)}$), whereas the HCO_3^- concentration remains essentially unchanged, demonstrating that
384 reservoir conditions (i.e., calcite and dolomite equilibrium) can be obtained by solely adding CO_2
385 that was lost due to degassing during upflow.

386

387 **4.3. Fluid inclusions**

388

389 *4.3.1. Petrography*

390 Fluid inclusions were found in calcite crystals in scales collected from the coated and
391 uncoated section of the casing as well as from the pump. A detailed petrographic investigation
392 was performed on scales collected from casing tubes #30 (coated, 341 m depth) and #62
393 (uncoated, 717 m depth) as well as from the first stage of the pumping system (808 m depth).
394 Four types of inclusions were observed at room temperature in scales from the two casing types
395 (Fig. 7): (i) colorless, single-phase gas inclusions that do not fluoresce under UV epi-
396 illumination, (ii) colorless petroleum inclusions that consist of ~80 vol% liquid + ~20 vol%
397 immiscible gas and that fluoresce light blue under UV epi-illumination, (iii) rarer light yellow-
398 brown petroleum inclusions containing ~80 vol% hydrocarbon liquid + ~20 vol% immiscible gas
399 and that exhibit yellow-orange fluorescence under UV epi-illumination; (iv) inclusions that are
400 mixtures of types i and ii, i.e. with 10–30 vol% blue-fluorescing liquid + 70–90 vol% immiscible
401 gas bubbles. Types i and ii are the most abundant. All four types of inclusions are distributed
402 throughout the crystals, indicating that they were trapped simultaneously during crystal growth,
403 i.e. they are all primary inclusions. No healed fractures were found (which could possibly host
404 secondary fluid inclusions) and no aqueous fluid inclusions were found, presumably owing to the
405 slow growth rate of calcite. In contrast to scales from the casing, calcite crystals precipitated at
406 the first stage of the pumping system host only petroleum inclusions showing blue or brownish
407 fluorescence under UV epi-illumination, whereas single-phase gas inclusions are absent.
408 Moreover, the calcite crystals precipitated at the pump contain smaller and far fewer inclusions
409 than crystals precipitated along the casing.

410 The occurrence of gas inclusions has important implications because it demonstrates that
411 a free gas phase is present within the production well. Further, the occurrence of petroleum

412 inclusions implies that immiscible oil droplets are present as well. The type (iv) inclusions
413 consisting of mixtures of variable amounts of gas and oil are expected when both end-member
414 phases coexist during inclusion entrapment (Diamond, 2003a). It is likely that these inclusions
415 derived from a minor influx of oil from petroleum pockets in the Jurassic carbonates (e.g.,
416 Malm) and/or overlying Cenozoic units of the Bavarian Molasse Basin (Mayrhofer et al., 2014;
417 Veron, 2005).

418 In summary, the simultaneous presence of gas inclusions and petroleum inclusions shows
419 that the produced fluid at Kirkstockach is actually a 3-phase mixture of mutually saturated water
420 + gas + oil. The total fraction of free gas is likely to be low, as gas bubbles are seen only
421 occasionally in the viewing port at the wellhead. Similarly, the oil fraction must also be low, as
422 minor petroleum films are only seldom observed during fluid sampling at the wellhead.

423

424 *4.3.2. Microthermometry*

425 No phase transitions were observable in the type-(i) gas inclusions. Only type-(ii) and -
426 (iii) petroleum inclusions (with ~20 vol.% gas bubbles) were measured. All undergo bubble-
427 point transitions, i.e. the gas bubble shrank progressively upon heating and dissappeared at the
428 temperature recorded as the homogenizaton temperature (T_h), whereupon the inclusions
429 consisted entirely of hydrocarbon liquid. None of these inclusions showed a change in absolute
430 size of their gas bubbles after their first heating to T_h and cooling back to room temperature. All
431 the homogenizaton temperatures (T_h) were reproducible on individual inclusions. These two
432 findings rule out stretching of the inclusions despite the ~30–90 bar rise in internal pressure upon
433 heating from room temperature to T_h. It follows that the T_h results can be considered
434 representative of the properties of the production fluid.

435 The T_h of inclusions within calcite crystals precipitated along the first stage of the
436 pumping system (808 m depth), along casing tube #62 (717 m depth) and along tube #30 (341 m
437 depth) are 128.2 ± 6.4 °C (n = 3), 130.7 ± 7.8 °C (n = 8) and 137.6 ± 1.5 °C (n = 5), respectively.
438 No systematic difference in T_h was observed between blue- and brown-fluorescing petroleum
439 inclusions.

440 The facts that the four inclusion types are coeval, they were trapped in a heterogeneous
441 (i.e. multi-phase) state and their host crystals behave rigidly (isochorically) during
442 microthermometry, lead to straightforward interpretations of the T_h values (see Diamond, 2003a,
443 2003b for the principles). A first case is the scale sample at tube #30 (~460 m above the pump),
444 in which petroleum was clearly saturated with respect to a free gas phase during entrapment. It
445 follows that the measured T_h values (137.6 ± 1.5 °C) must correspond directly to the trapping
446 temperature of the inclusions. Indeed, as expected from theory, the results precisely match the
447 137 °C temperature of the production fluid inferred for tube #30 when taking into account the
448 minor temperature decrease occurring in the production well during upflow. The second case is
449 the scale sample from the pump, in which no gas inclusions were found. Theory dictates that the
450 measured T_h values (128.2 ± 6.4 °C) must be lower than the trapping temperature of the
451 inclusions. While this expected behavior is confirmed by the results (T_{fluid} at the pump is
452 estimated at 137.6 °C), the small difference between T_h and $T_{trapping}$ (3–16 °C) suggests the
453 petroleum was close to saturation with respect to a free gas phase. The third case is the sample
454 from tube #62, some 80 m above the pump. Here gas inclusions are present and the highest T_h
455 values match the temperature of the production fluid precisely, but other T_h values are up to 15
456 °C lower, suggesting slight undersaturation with respect to gas, as observed at the pump. These

457 results suggest increasing gas saturation with height above the pump and they rule out the
458 possibility that the production fluid was overheated near the pump.
459
460 *4.3.2. Crushing and gas analyses*
461 The composition of gas inclusions liberated from fluid inclusions during crushing of
462 calcite scalings is fairly constant (Table 3). Gases liberated from all four samples mainly consist
463 of N_2 and minor CO_2. Methane and other hydrocarbon gases are present only in trace amounts.
464 The N_2/CO_2 ratio varies from 2.4 to 6.9, but no clear trend with sampling depth is observed. It
465 should be noted that H_2O gas was not analyzed and that the values listed in Table 3 would have
466 to be scaled to lower values if it were actually present in the inclusions. The N_2/CO_2 ratio,
467 however, would remain the same. Since N_2 gas can be liberated by the degradation of organic
468 matter (Littke et al., 1995), the observed high N_2 gas concentrations likely originate from the
469 same hydrocarbon source as the petroleum inclusions (Fig. 7).
470
471 **5. DISSCUSION**
472
473 **5.1. Scenarios for scaling formation**
474 The presence of Fe corrosion phases as well as CO_2-bearing gas inclusions demonstrate
475 that corrosion of the uncoated casing and CO_2 degassing of the thermal water are occurring in the
476 production well. Equations 4 and 5 illustrate that both processes are associated with a *pH*
477 increase due to the consumption of protons (i.e., H^+):
478
479 $$Fe^0_{(s)} + 2H^+ \rightarrow Fe^{2+} + H_2 \quad (4)$$

480 $HCO_3^- + H^+ \rightarrow CO_{2(g)} + H_2O$ (5)

481

482 Since calcite solubility decreases with increasing *pH*, corrosion as well as CO_2 degassing
483 promote the precipitation of calcite in the production well. In addition, calcite precipitation is
484 favored by decompression during upflow in the well (Figs. 2, 4). Based on these processes
485 identified to promote calcite precipitation (i.e., pressure drop, corrosion, CO_2 degassing) we
486 propose 4 scenarios for the formation of the calcite-dominated scalings (Fig. 8):

487 (i) Linear decompression scenario: the precipitation of calcite is controlled by the
488 solubility decrease associated with the pressure drop of ca. 280 bar occurring when
489 the thermal water is pumped from the Malm aquifer to the surface.

490 (ii) Corrosion scenario: the precipitation of calcite is controlled by the corrosion of the
491 casing and the associated increase in *pH* and decrease in calcite solubility.

492 (iii) Gas influx scenario: the precipitation of calcite is controlled by an influx of a free gas
493 phase into the production well, which based on gas analyses of crushed fluid
494 inclusions is dominated by N_2. As a consequence, CO_2 dissolved in the thermal water
495 may be stripped into the gas phase, inducing a *pH* increase (Eq. (5)) and hence a
496 decrease in calcite solubility.

497 (iv) Gas exsolution scenario: the precipitation of calcite is controlled by boiling of the
498 produced thermal water within the pump at 800 m depth within the production well,
499 due to a major, non-hydrostatically controlled pressure drop or to a major temperature
500 increase.

501

502 **5.2. Assessing the scaling formation scenarios**

503

504 *5.2.1. Linear decompression scenario*

505 Aqueous speciation calculations using the reconstructed reservoir fluid yield a change in
506 the calcite saturation index of 0.16 when the pressure drops from 300 to 18 bar in the production
507 well while the temperature is decreasing from about 140 to 135 °C (Table 2, "Linear *P*-drop
508 scenario"). This calculation demonstrates that despite the rather low sensitivity of calcite
509 solubility to pressure variations (Fig. 4) and the minor temperature drop occurring in the
510 production well, decompression of the reservoir fluid may yield a notable calcite supersaturation
511 at the wellhead. However, the increase in $SI_{calcite}$ associated with decompression is significantly
512 lower than the maximum value computed for the wellhead samples ($SI_{calcite}$ = 0.30, Table 2).
513 Moreover, calcite precipitation induced by decompression would reset the saturation index to
514 zero, but this conflicts with the observation that certain wellhead samples are undersaturated with
515 respect to calcite (Table 2). Finally, the linear decompression scenario does not consider the
516 presence of a free gas phase in the production well, which is clearly demonstrated by our fluid
517 inclusion evidence (Fig. 7). This means that calcite precipitation constitutes the only DIC sink in
518 this scenario. Numerically fixing the calcite saturation index to zero by removing equal amounts
519 of Ca^{2+} and HCO_3^- during decompression decreases the Ca^{2+} and DIC concentrations in the
520 production well by 0.13 mmol/kg_{H2O} due to calcite precipitation (Table 2, "linear *P*-drop +
521 calcite prec."). The decrease in DIC accounts for only 13 mol.% of the amount that had to be
522 numerically added to reconstruct the water composition at reservoir conditions. It follows that
523 another process is controlling the DIC content and that decompression between the reservoir and
524 the wellhead cannot be the sole driver for scaling formation within the production well.

525

526 *5.2.2. Corrosion scenario*

527 The proportion of typical corrosion products such as Fe oxides and Fe sulfides in scalings
528 sampled along the production well is rather low (Table 1). Most importantly, these corrosion
529 phases occur only at the interface to the uncoated casing, implying that corrosion accompanies
530 only the initial stage of calcite scaling. Once the casing is covered (i.e., passivated) by calcite,
531 corrosion is slowed down because the casing is no longer in contact with the upflowing thermal
532 water. Moreover, scaling occurs along the coated tubes as well, which are unaffected or only
533 slightly affected by corrosion (Table 1). Similarly, in analogy to the linear decompression
534 scenario, the corrosion scenario does not consider the presence of a free gas phase in the
535 production well, as inferred from fluid inclusion analyses (Fig. 7). In summary, corrosion is
536 unlikely to have been the main driver for scaling formation within the production well.

537

538 *5.2.3. Gas influx scenario*

539 In contrast to the two previous scenarios, this one considers the presence of a free gas phase in
540 the upflowing thermal water and it is thus consistent with the presence of gas inclusions within
541 calcite crystals (Fig. 7), as well as with the need to numerically add CO_2 in order to reconstruct
542 the composition of the reservoir fluid. If N_2, which constitutes the major component of the gas
543 inclusions (Table 3), entered the production well as a free gas phase (Fig. 8c), it would strip
544 dissolved CO_2 from the thermal water as it approaches gas–water chemical equilibrium. Since
545 CO_2 stripping is associated with a *pH* increase (Eq. (5)), it would immediately lower the
546 solubility of calcite in the upflowing thermal water. Accordingly, the influx of a free gas phase
547 into the base of the production well could cause significant calcite supersaturation and possibly
548 drive scaling. The problem with this scenario, however, is that the concentration of major gases

549 dissolved in wellhead samples (CO_2, CH_4, N_2) are several orders of magnitude lower than the
550 equilibrium concentration at the reservoir pressure of 300 bar (Table 2). This implies that the gas
551 influx scenario is only possible if an N_2–CO_2-rich gas phase somehow ingressed from a separate
552 reservoir that is hydrologically decoupled from the Malm aquifer, with partial mixing of the gas
553 and water first occurring near to or within the production well. If there were a hydrological
554 connection between the postulated gas reservoir and the Malm aquifer, the dissolved
555 concentration under reservoir conditions would correspond to the equilibrium concentration
556 under reservoir *P–T* conditions (300 bar, 140°C). Such an unusual, localized plumbing
557 configuration could perhaps be imagined for the Kirchstockach site, but the fact that substantial
558 scaling is observed in two thirds of the geothermal plants SE of Munich demonstrates that the
559 phenomenon is not just local. Therefore, we consider influx of a disequilibrium gas an unlikely
560 scenario for scaling as well.
561
562 *5.2.4. Gas exsolution scenario*
563 Similar to the gas influx scenario, the gas exsolution scenario is consistent with the
564 presence of gas inclusions within calcite crystals (Fig. 7). The difference is that this scenario
565 considers the formation of the free gas phase within the production well itself (Fig. 8d) and not
566 within the geothermal reservoir. Boiling could in principle be induced by overheating of the
567 pump at 800 m depth prior to scaling formation, although the water would have to reach about
568 250 °C at that depth to intersect the gas-saturation curve, which seems unlikely at flow rates of
569 ~2 m/s. In fact, significant heating of the water seems to be ruled out because the gas-saturated
570 fluid inclusions at the pump depth homogenize below 138 °C, and because the orthorhombic

polymorph of bornite, which is stable only below 200 °C, occurs as a corrosion product on the pump itself.

This leaves only a major pressure drop, e.g. due to fast operation of the pump impeller, as a conceivable cause of gas exsolution. To assess whether such a pressure drop is a feasible scenario, boiling calculations were performed using CHILLER. Simulations were run using the reconstructed reservoir fluid (Table 2) as initial composition and by continuously lowering the pressure at a constant temperature of 137 °C, corresponding to the inferred trapping temperature of the gas inclusions, until the saturation pressure of pure water was reached (3.3 bar). In addition, based on the finding that the gas inclusions have high N_2 to CO_2 ratios (Table 3), simulations were run for variable initial N_2 concentrations in order to reconstruct the dissolved N_2 concentration prior to gas exsolution. The behavior of methane and other gases was not simulated because they are present only in traces in the gas inclusions.

Simulated boiling of the reservoir fluid in the production well

Figure 9 illustrates that the composition of the exsolved gas as well as the remaining liquid phase depends on the dissolved N_2 concentration at reservoir conditions. If the reservoir N_2 concentration is equal to the maximum N_2 concentrations measured at the wellhead (1 $mmol/kg_{H2O}$, Table 2), degassing starts at about 5.5 bar and the gas phase consists of mainly steam (H_2O) and minor amounts of N_2 and CO_2. In contrast, if the N_2 concentration in the reservoir is 3 or 5 times larger, degassing starts at 9 and 14 bar, respectively, and the gas phase is initially dominated by N_2. With progressive degassing (i.e., decreasing pressure), the steam fraction increases while the N_2 fraction decreases. In contrast, the CO_2 fraction of the gas phase shows only minor variations at pressures > 4 bar, which means that CO_2 is continuously stripped

594 into the gas phase. Degassing of N_2 and CO_2 yields a *pH* increase as well as decreases in DIC
595 and N_2 concentrations in the liquid phase. As a consequence, calcite becomes significantly more
596 supersaturated than in the linear decompression scenario (Table 2) and its saturation index
597 increases with continued degassing. The dependence of the aqueous composition on the initially
598 dissolved N_2 concentration is such that at a specific pressure, *pH* and calcite saturation index
599 correlate positively with the reservoir N_2 concentration, while the DIC concentration correlates
600 negatively. These correlations occur because, owing to the low N_2 solubility in aqueous fluids,
601 high reservoir N_2 concentrations yield an increase of the gas saturation pressure and thus a higher
602 gas fraction at a specific degassing pressure.

603 In general, our boiling simulations (Fig. 9) simultaneously reproduce the ranges of
604 parameters measured on wellhead samples (e.g., *pH*, DIC, $SI_{calcite}$, $[N_{2(aq)}]$), but only at low
605 degassing pressures of 4–6 bar. The same applies for the N_2/CO_2 ratios of the gas inclusions. The
606 composition of the wellhead sample that appears to be least affected by scale formation (i.e.,
607 max. [Ca] and max. $SI_{calcite}$, Table 2: KST-12) is nicely approximated at a degassing pressure of
608 4.6 bar by setting the reservoir N_2 concentration to 3 mml/kg (Table 4). A unique reconstruction
609 of the reservoir N_2 concentration, however, is not possible because other combinations of
610 reservoir N_2 concentrations and degassing pressures can yield similar fits as long as the
611 degassing pressure is < 6 bar.

612

613 *Implications for the Kirchstockach geothermal power plant*

614 Based on the observations that wellhead concentrations and N_2/CO_2 ratios of gas
615 inclusions are closely approximated by our boiling calculations (Table 4), we postulate the
616 following sequence of processes to explain calcite scaling at Kirchstockach:

1. Carbonate minerals and fluid are at thermodynamic equilibrium within the Malm aquifer owing to high reaction rates and sufficiently long residence times. As a consequence, thermal water that is pumped into the well at 3300–3900 m depth (Fig. 2a,b) is saturated with respect to calcite and dolomite (i.e., $SI_{calcite} = SI_{dolomite} = 0$).
2. Decompression of the fluid during upflow within the production well induces notable calcite supersaturation (Table 2) that may trigger calcite precipitation well below the intake of the pump.
3. A major pressure drop to 4–6 bar occurs somewhere in the production well. This pressure is far below the operational pressure of the plant at the surface (16-18 bar) and far below the pressure at the intake of the pump (ca. 50 bar, Fig. 2b,c). The interior of the pump is the only location within the geothermal loop where such a low pressure is imaginable (Fig. 2c). Therefore, we hypothesize that fast rotation of the impeller in the pump induces a highly localized pressure drop and subsequent exsolution of gas consisting of mainly steam and N_2 (Fig. 9). Such gas exsolution within centrifugal pumps is a known phenomenon called cavitation (Rayner, 1995), and it has been described for similar liquid-dominated geothermal systems but at shallower pump installation depths than that at the Kirchstockach geothermal site (Aksoy, 2007; Aksoy et al., 2008).
3. Perturbation of the saturation states of calcite and dolomite. Upon exsolution of N_2 and steam at the pump, aqueous CO_2 is partially stripped into the gas phase (Fig. 9g-i), immediately causing an increase in calcite and dolomite supersaturation ($SI >> 0$, Fig. 9d). This triggers calcite precipitation or alternatively accelerates on-going calcite precipitation, whereas dolomite fails to precipitate owing to kinetic limitations (see rate compilation by Palandri and Kharaka, 2004).

4. Persistence of calcite supersaturation and subsequent scaling at the pump, along the casing and within the geothermal plant at the surface. Scales form along the entire pump casing (Fig. 5) because the observed calcite precipitation rate along the uppermost 800 m of the casing (7.12×10^{-13} mol/L/s) is too slow to set the produced thermal water back to calcite saturation. Similarly, redissolution of gaseous CO_2 potentially occurring when the pressure increases to about 100 bar above the pump is too slow to reattain equilibrium. Therefore, CO_2 remains at least partly in the gas phase, as demonstrated by the presence of CO_2-bearing gas inclusions at shallow depths in the well (Fig. 7, Table 3). Consequently, wellhead samples are still supersaturated with respect to calcite (Table 2), which explains why scaling is currently ongoing in the geothermal plant at the surface (Fig. 3c).

Open questions

While our calculations nicely predict many of our observations by invoking boiling of the reconstructed reservoir fluid at 4–6 bar (Fig. 9, Table 4), they predict gas volume fractions of up to 10%, which is certainly higher than the gas fraction observed at the wellhead. Consequently, a fraction of the gas phase must redissolve into the aqueous phase before reaching the wellhead to yield wellhead gas fractions lower than those at the pump. In contrast, some of the CO_2 must remain in the gas phase to maintain calcite supersaturation and to form gas inclusions as discussed above. Dissolution of CO_2 gas is in fact notoriously slow at $T < 150$ °C and this phenomenon has long plagued solubility experiments in pure water and in salt solutions (e.g. as reviewed by Diamond and Akinfiev, 2003; Akinfiev and Diamond, 2010). Experimentalists typically allow anywhere between 30 minutes and several hours to equilibrate percolating CO_2

663 gas with aqueous solutions, even in small-volume containers equipped with mechanical stirrers
664 (e.g. Malinin and Savelyeva, 1972). In the production well at Kirchstockach, gas bubbles take
665 only ~7 min. to rise from the pump to the surface plant. Partial rather than complete, CO_2
666 equilibration is therefore to be expected.

667 At Kirchstockach there is no possibility to closely monitor the pump in order to verify the
668 occurrence of boiling and gas redissolution related to cavitation and the subsequent pressure
669 increase above the pump. However, based on the rather wide variety of internally consistent
670 observations at hand (gas inclusions, absence of temperature increase in the production well,
671 geochemical modeling vs. wellhead fluid compositions, experimental degassing pressures) the
672 pressure has to be as low as 4–6 bar somewhere within the production well and we are confident
673 that cavitation at the pump is the most likely reason. Furthermore, our observations demonstrate
674 that boiling and gas redissolution are highly dynamic. For instance, three of our 13 wellhead
675 samples are undersaturated with respect to calcite (Table 2, Fig. 6a), which can only happen if
676 calcite precipitation upon boiling occurs fast enough to set the calcite saturation index back to
677 zero, and if some redissolution of CO_2 takes place during further upflow in the production well.
678 Finally, variations in Ca^{2+} and HCO_3^- concentrations observed at the wellhead (Fig. 6)
679 demonstrate that calcite precipitation rates along the production well are highly variable. The
680 actual reason for the varying precipitation rate is not yet resolved, although it might be related to
681 flow turbulences within the well and/or to a varying CO_2 redissolution rate above the pump.

682 Unfortunately, we do not know if and to what extent scaling has occurred at greater
683 depths below the pump. However, once this is known, it should be possible using our approach
684 to assess whether decompression plays a significant role next to cavitation in controlling scale
685 formation within the production well and in the geothermal plant at the surface.

686

687 **6. SUMMARY AND CONCLUSIONS**

688 We have presented an extensive geochemical dataset from the Kirchstockach geothermal
689 well, including chemical analyses of wellhead samples, chemical and mineralogical analyses of
690 scales, as well as analyses of fluid inclusions trapped in the scales, to unravel the causes of
691 substantial amounts of calcite scaling. Geochemical modeling shows that the calcite solubility
692 decrease associated with decompression of the produced thermal water along the hydrostat
693 during flow from the reservoir to the wellhead cannot fully explain calcite supersaturation
694 observed at the wellhead, suggesting that another process is driving scaling as well. Only minor
695 amounts of pyrrhotite and magnetite scales are present, implying that corrosion of the casing is
696 limited and hence its influence on calcite solubility is negligible. The occurrence of N_2-rich gas
697 inclusions demonstrate that a free gas phase is present within the well, from the surface down to
698 at least the depth of the downhole-pump (800 m). Stripping of CO_2 from the thermal water by
699 this gas phase is calculated to lower calcite solubility significantly, and it is therefore the most
700 likely cause of scaling in addition to decompression. An origin of the gas in the reservoir seems
701 unlikely based on the hydrogeological setting, because at the reservoir level the gas would have
702 to be out of equilibrium with the thermal water to explain the available chemical analyses.
703 Boiling of the produced water within the geothermal well is the most plausible mechanism to
704 generate the gas phase.

705 Boiling calculations using CHILLER successfully predicted the chemical composition of
706 wellhead samples as well as the N_2/CO_2 ratios of gas inclusions when the boiling pressure was
707 set to a low pressure of 4–6 bar. As the downhole pump is the only location within the
708 geothermal loop where such a low pressure is imaginable, we hypothesize that fast rotation of the

centrifugal impeller induces cavitation, generating the gas phase which leads to CO_2-stripping and hence accelerating scaling. It follows that scaling and its related technical problems could be limited if the pump is operated at lower production rates and/or if the well design at the pump is optimized to avoid cavitation.

ACKNOWLEDGMENTS

The Swiss Competence Center of Energy Research – Supply of Electricity (SCCER-SoE) supports research in geothermal energy at the University of Bern. Mark Reed and Nic Spycher kindly provided us a copy of CHILLER. Special thanks go to Lukas Aschwanden for assisting CW in the fluid inclusion lab and to Arthur Adams for electron microprobe analyses. We also appreciate the analytical support of Andrej Voropaev and Stephan Wechner (Hydroisotop) and the on-site help from Holm Bremer and Igor Hajdu. Finally, we thank the editor, Eva Schill, and two anonymous reviewers for their constructive comments that greatly improved the manuscript.

FIGURE CAPTIONS

Figure 1:

Geographical and geological overview of the studied site. (a) Relief map showing the location of the geothermal plant at Kirchstockach. (b) Schematic cross section through the Bavarian Molasse Basin illustrating that the Malm aquifer dips southward and that geothermal wells are aimed to intersect permeable fracture zones (modified from Mayrhofer et al., 2014).

Figure 2:

Schematic of the production well of the geothermal plant at Kirchstockach, illustrating (a) the vertical well profile including a simplified overview of the stratigraphy; (b) the detailed well and pump design (projected into the vertical axis); (c) the idealized pressure profile corresponding to the situation where the intake of the pump is placed 800 m below the surface.

Figure 3:

Photographs of scales formed at (a) the pump, (b) along the pump casing and (c) in installations of the geothermal plant at the surface.

Figure 4:

Log(*K*) of calcite–fluid equilibrium ($CaCO_3 + H^+ = HCO_3^- + Ca^{2+}$) as a function of pressure and temperature, illustrating that calcite solubility is strongly dependent on temperature and only weakly dependent on pressure. Symbols denote log(*K*) values tabulated in the Soltherm.H06 database (Reed and Palandri, 2006), whereas solid lines refer to the interpolation calculated by TOUGHREACT according to Eqs. (1) and (2) as well as the parameters listed in Table S2 (supporting information).

Figure 5:

Depth-dependent thickness of calcite scales along the pump casing. The scales precipitated during the investigated operational period from December 2014 to March 2015. Bars denote the thickness of scaling on each of the 68 casing tubes.

Figure 6:

Variation in compositions of wellhead fluids collected between October 2014 and September 2015. *SI*: saturation index. TDS: total dissolved solids. (a,b,c) Linear correlations between the calcite saturation index and TDS, Ca^{2+} and TDS, and HCO_3^- and TDS. (d) Demonstration that other major species (Na^+, Cl^-) do not contribute to the observed TDS variation.

Figure 7:

Examples of primary gas and petroleum inclusions observed in calcite crystals that precipitated along tube #30. Microphotographs (a) and (c) taken under normal transmitted light. Microphotographs (b), (d) and (e) taken under UV reflected light. (b) and (d) show the same fields of view as (a) and (c), demonstrating that the petroleum inclusions are fluorescent, whereas the gas inclusions are not. (e) Petroleum inclusions showing both orange and blue fluorescence.

Figure 8:

Scenarios of the formation of calcite scaling: (a) linear decompression scenario in which calcite precipitation occurs only due to the solubility decrease associated with the linear pressure decrease of ca. 280 bar as the thermal water is pumped from the Malm aquifer to the surface; (b) Corrosion scenario in which calcite precipitation is induced by corrosion of the casing, which increases pH and hence lowers calcite solubility; (c) Gas influx scenario in which calcite precipitation is controlled by influx of an N_2-rich gas phase into the production well which subsequently strips CO_2 from the thermal water; (d) Gas exsolution scenario in which calcite precipitation is caused by gas exsolution from the produced thermal water due to a localized pressure drop, most likely located within the centrifugal pump.

Figure 9:

Simulated evolution of properties of the liquid and the coexisting gas phase exsolving from the reconstructed reservoir fluid (Table 2) when the pressure decreases to the steam-saturation pressure (P_{sat} = 3.3 bar) at T = 137 °C and at variable N_2 concentrations. (a) Gas fraction. (a) *pH*. (b) Dissolved organic carbon (DIC) concentration. (c) Calcite saturation index. (d) Dissolved N_2 concentration. (f) Volumetric N_2/CO_2 ratio. (g)–(i) Gas composition. Gray bands show the range of the *y*-axis parameter measured in wellhead fluid samples ((b–e), Table 2) or in gas inclusions ((f), Table 3).

REFERENCES

Akinfiev, N. N., Diamond, L. W., 2010. Thermodynamic model of aqueous CO_2–H_2O–NaCl solutions from −22 to 100 °C and from 0.1 to 100 MPa. Fluid Phase Equilibria 295, 104-124

Aksoy, N., 2007. Optimization of downhole pump setting depths in liquid-dominated geothermal systems: A case study on the Balcova-Narlidere field, Turkey. Geothermics 36, 436-458.

Aksoy, N., Serpen, U., Filiz, Ş., 2008. Management of the Balcova–Narlidere geothermal reservoir, Turkey. Geothermics 37, 444-466.

Ámannsson, H., 1989. Predicting calcite deposition in krafla boreholes. Geothermics 18, 25-32.

Arnórsson, S., 1989. Deposition of calcium carbonate minerals from geothermal waters — theoretical considerations. Geothermics 18, 33-39.

Benoit, W. R., 1989. Carbonate scaling characteristics in Dixie Valley, Nevada geothermal wellbores. Geothermics 18, 41-48.

Bozau, E., Häußler, S., van Berk, W., 2015. Hydrogeochemical modelling of corrosion effects and barite scaling in deep geothermal wells of the North German Basin using PHREEQC and PHAST. Geothermics 53, 540-547.

Cacace, M., Blöcher, G., Watanabe, N., Moeck, I., Börsing, N., Scheck-Wenderoth, M., Kolditz, O., Huenges, E., 2013. Modelling of fractured carbonate reservoirs: outline of a novel technique via a case study from the Molasse Basin, southern Bavaria, Germany. Environ Earth Sci 70, 3585-3602.

Diamond, L. W., 2003a. Systematics of H_2O inclusions, in: Samson, I., Anderson, A. and Marshall, D. (Eds.), Fluid Inclusions: Analysis and Interpretation. Mineralogical Association of Canada. Short Course Volume 32, 55-79.

Diamond, L. W., 2003b. Introduction to gas-bearing, aqueous fluid inlcusions, in: Samson, I., Anderson, A. and Marshall, D. (Eds.), Fluid Inclusions: Analysis and Interpretation. Mineralogical Association of Canada. Short Course Volume 32, 101-158.

Diamond, L. W., Akinfiev, N. N., 2003. Solubility of CO_2 in water from −1.5 to 100 °C and from 0.1 to 100 MPa: evaluation of literature data and thermodynamic modelling. Fluid Phase Equilibria 208, 265-290.

Dussel, M., Lüschen, E., Thomas, R., Agemar, T., Fritzer, T., Sieblitz, S., Huber, B., Birner, J., Schulz, R., 2016. Forecast for thermal water use from Upper Jurassic carbonates in the Munich region (South German Molasse Basin). Geothermics 60, 13-30.

Dublyansky, Y.V., 2012, Design of two crushing devices for release of the fluid inclusion volatiles: Central European Journal of Geosciences 4, 219–224.

Eichinger, F., Meier, D. B., Hämmerli, J., Diamond, L. W., 2010. Stable isotope signatures of gases liberated from fluid inclusions in bedrock at Olkiluoto. Posiva Working Report 2010-88. Olkiluoto, Finnland.

Gallup, D. L., 1989. Iron silicate scale formation and inhibition at the salton sea geothermal field. Geothermics 18, 97-103.

García, A. V., Thomsen, K., Stenby, E. H., 2006. Prediction of mineral scale formation in geothermal and oilfield operations using the Extended UNIQUAC model: Part II. Carbonate-scaling minerals. Geothermics 35, 239-284.

Grguric, B. A., Putnis, A., Harrison, R. J., 1998. An investigation of the phase transitions in bornite (Cu_5FeS_4) using neutron diffraction and differential scanning calorimetry. American Mineralogist 83, 1231-1239.

Gunnarsson, I., Arnórsson, S., 2005. Impact of silica scaling on the efficiency of heat extraction from high-temperature geothermal fluids. Geothermics 34, 320-329.

Hämmerli, J., 2009. Gas-rock interaction at the Olkiluoto Investigation Site, Finland, Msc Thesis, University of Bern, Switzerland.

Helgeson, H. C., Kirkham, D. H., Flowers, G. C., 1981. Theoretical prediction of the thermodynamic behavior of aqueous electrolytes by high pressures and temperatures; IV, Calculation of activity coefficients, osmotic coefficients, and apparent molal and standard and relative partial molal properties to 600 °C and 5kb. Am. J. Sci. 281, 1249-1516.

Honegger, J. L., Czernichowski-Lauriol, I., Criaud, A., Menjoz, A., Sainson, S., Guezennec, J., 1989. Detailed study of sulfide scaling at la courneuue nord, a geothermal exploitation of the Paris Basin, France. Geothermics 18, 137-144.

Kristmannsdóttir, H., 1989. Types of scaling occurring by geothermal utilization in Iceland. Geothermics 18, 183-190.

Lentsch, D., Dorsch, K., Sonnleitner, N., Schubert, A. (2015). Prevention of Casing Failures in Ultra-Deep Geothermal Wells (Germany). Proceedings, World Geothermal Congress, Melbourne, Australia, 19-25 April 015.

Lindal, B., Kristmannsdóttir, H., 1989. The scaling properties of the effluent water from Kizildere power station, Turkey, and recommendation for a pilot plant in view of district heating applications. Geothermics 18, 217-223.

Littke, R., Krooss, B., Idiz, E., Frielingsdorf, J., 1995. Molecular nitrogen in natural-gas accumulations - generation from sedimentary organic-matter at high-temperatures. Aapg Bulletin 79, 410-430.

Malinin, S. D., Saveleva, N. I., 1972. Exerimental investigatioin of CO_2 solubility in NaCl and $CaCl_2$ solutions at temperatures of 25, 50 and 75 degrees and elevated CO_2 pressure. Geokhimiya 643-&.

Mayrhofer, C., Niessner, R., Baumann, T., 2014. Hydrochemistry and hydrogen sulfide generating processes in the Malm aquifer, Bavarian Molasse Basin, Germany. Hydrogeology Journal 22, 151-162.

McLimans, R. K., 1987. The application of fluid inclusions in migration of oil and diagenesis in petroleum reservoirs: Applied Geochemistry 2, 585–603.

Moeck, I., Mraz, E., 2015. Multiphase fossil normal faults in geothermal systems: Insights from the Bavarian Molasse Basin. Geotectonic Research70-72.

Mundhenk, N., Huttenloch, P., Sanjuan, B., Kohl, T., Steger, H., Zorn, R., 2013. Corrosion and scaling as interrelated phenomena in an operating geothermal power plant. Corrosion Science 70, 17-28.

Palandri, J. L., Kharaka, Y. K., 2004. A compilation of rate parameters of water-mineral interaction kinetics for application to geochemical modeling, US Geological Survey. Report 2004-1068.

Rayner, R., 1995. Pump Users Handbook. Elsevier Advanced Technology, Oxford, UK, 427 pp.

Reed, M., 1992. Calculation of multicomponent chemical equilibria and reaction progress in systems involving minerals, gases and aqueous phase. Geochimica et Cosmochimica Acta 46, 513-528.

Reed, M., 1997. Hydrothermal alteration and its relationship to ore field composition, in: Barnes, H. L. (Eds.), Geochemistry of hydrothermal ore deposits. John Wiley & Sons, New York. 303-366.

Reed, M., 1998. Calculation of simultaneous chemical equilibria in aqueous-mineral-gas systems and its application to modeling hydrothermal processes., in: Richards, J. and Larson, P. (Eds.), Techniques in hydrothermal ore deposits geology. Reviews in Economic Geology 10, 109-124.

Reed, M., Palandri, J. L., 2006. SOLTHERM.H06, a database of equilibrium constants for minerals and aqueous species. Available from the authors, University of Oregon, Eugene, USA.

Reed, M., Spycher, N., 2006. Users Guide for CHILLER: a program for computing water-rock reactions, boiling, mixing and other reaction processes in aqueous mineral-gas systems. Available from the authors, University of Oregon, Eugene, USA.

Regenspurg, S., Feldbusch, E., Byrne, J., Deon, F., Driba, D. L., Henninges, J., Kappler, A., Naumann, R., Reinsch, T., Schubert, C., 2015. Mineral precipitation during production of geothermal fluid from a Permian Rotliegend reservoir. Geothermics 54, 122-135.

Scheiber, J., Seibt, A., Birner, J., Genter, A., Moeckes, W. (2013). Application of a Scaling Inhibitor System at the Geothermal Power Plant in Soultz-sous-Forêts: Laboratory and On-site Studies. Proceedings, European Geothermal Congress, Pisa, Italy, June 3-7.

Simmons, S. F., Christenson, B. W., 1994. Origins of calcite in a boiling geothermal system. Am. J. Sci. 294, 361-400.

Spycher, N. F., Reed, M. H., 1988. Fugacity coefficients of H_2, CO_2, CH_4, H_2O and of H_2O-CO_2-CH_4 mixtures: A virial equation treatment for moderate pressures and temperatures applicable to calculations of hydrothermal boiling. Geochim. Cosmochim. Acta 52, 739-749.

Steefel, C. I., Appelo, C. A. J., Arora, B., Jacques, D., Kalbacher, T., Kolditz, O., Lagneau, V., Lichtner, P. C., Mayer, K. U., Meussen, H., Molins, S., Moulton, D., Parkhurst, D. L., Shao, H., Simunek, J., Spycher, N., Yabusaki, S., Yeh, G. T., 2015. Reactive transport codes for subsurface environmental simulation. Computational Geoscience 19, 445-478.

Thomas, D. M., Gudmundsson, J. S., 1989. Advances in the study of solids deposition in geothermal systems. Geothermics 18, 5-15.

Truesdell, A. H., Singers, W., 1974. The calculation of aquifer chemistry in hot-water geothermal systems. Journal of Research of the US Geological Survey 2, 271-278.

Veron, J., 2005. The Alpine Molasse Basin - Review of petroleum geology and remaining potential. Bull. Angew. Geol. 10, 75-86.

Wilson, N., Webster-Brown, J., Brown, K., 2007. Controls on stibnite precipitation at two New Zealand geothermal power stations. Geothermics 36, 330-347.

Xu, T., Sonnenthal, E. L., Spycher, N., Zheng, L., 2014. TOUGHREACT V3.0-OMP Reference Manual: A Parallel Simulation Program for Non-Isothermal Multiphase Geochemical Reactive Transport. LBNL Manual http://esd.lbl.gov/FILES/research/projects/tough/documentation/TOUGHREACT_V3-OMP_RefManual.pdf.

Zarrouk, S. J., Woodhurst, B. C., Morris, C., 2014. Silica scaling in geothermal heat exchangers and its impact on pressure drop and performance: Wairakei binary plant, New Zealand. Geothermics 51, 445-459.

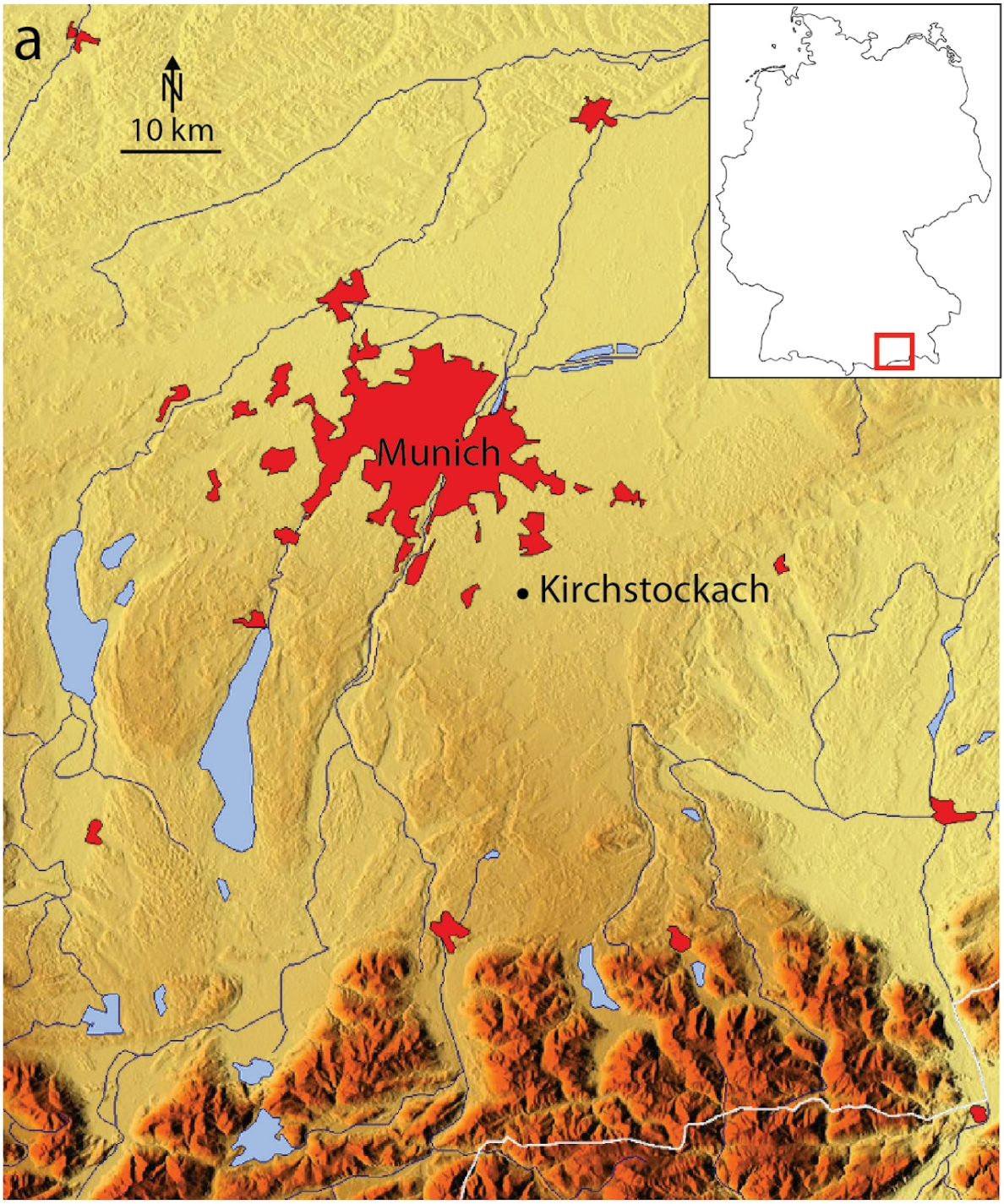
a
N
10 km
Munich
Kirchstockach

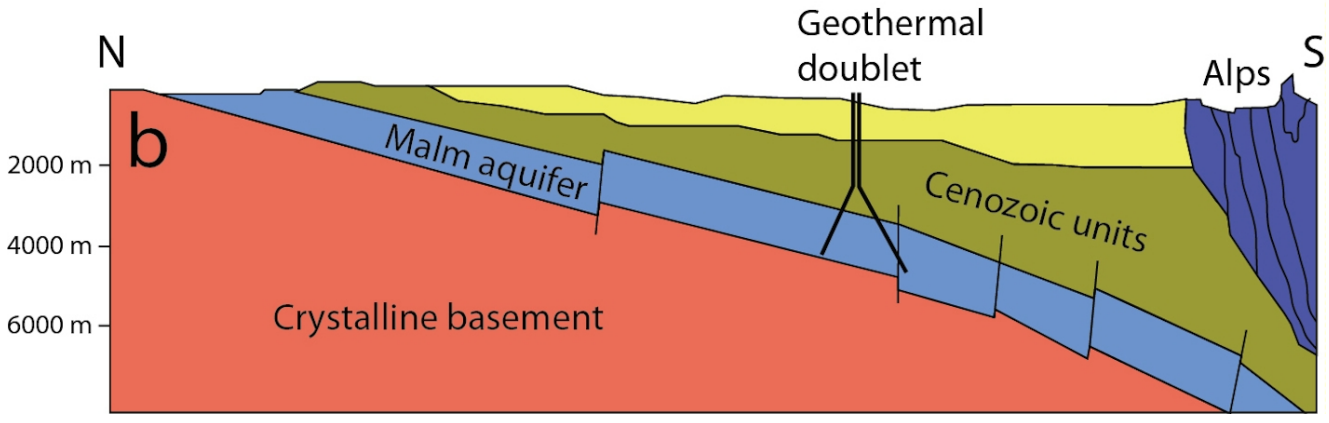
N
Geothermal
doublet
Alps
S
b
2000 m
4000 m
6000 m
Malm aquifer
Cenozoic units
Crystalline basement

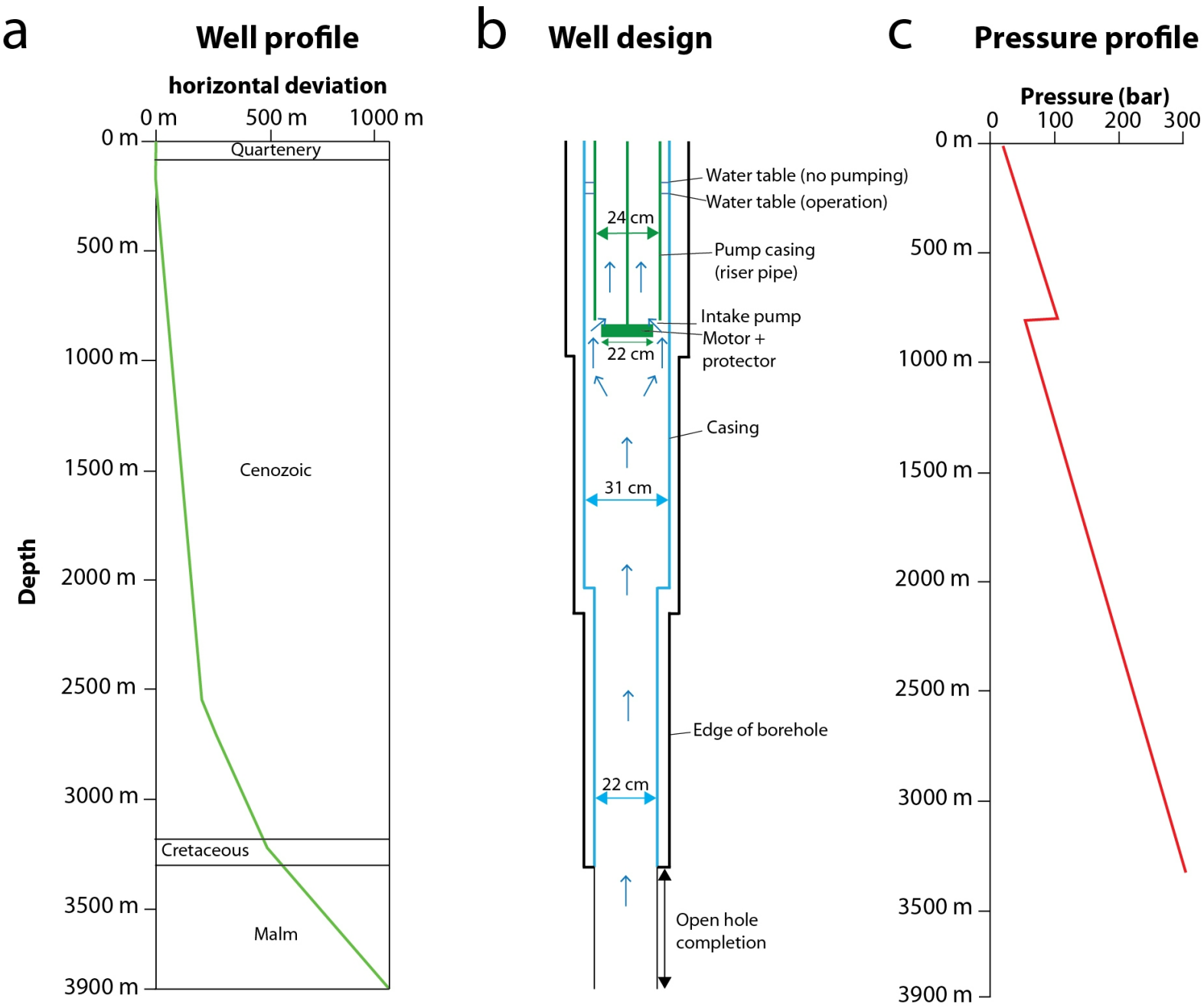
a
Well profile
horizontal deviation
0 m
500 m
1000 m
Depth
0 m
500 m
1000 m
1500 m
2000 m
2500 m
3000 m
3500 m
3900 m
Quartenery
Cenozoic
Cretaceous
Malm
b
Well design
Water table (no pumping)
Water table (operation)
24 cm
Pump casing
(riser pipe)
Intake pump
Motor +
protector
22 cm
Casing
31 cm
Edge of borehole
22 cm
Open hole
completion
c
Pressure profile
Pressure (bar)
0
100
200
300
0 m
500 m
1000 m
1500 m
2000 m
2500 m
3000 m
3500 m
3900 m

a

b

c

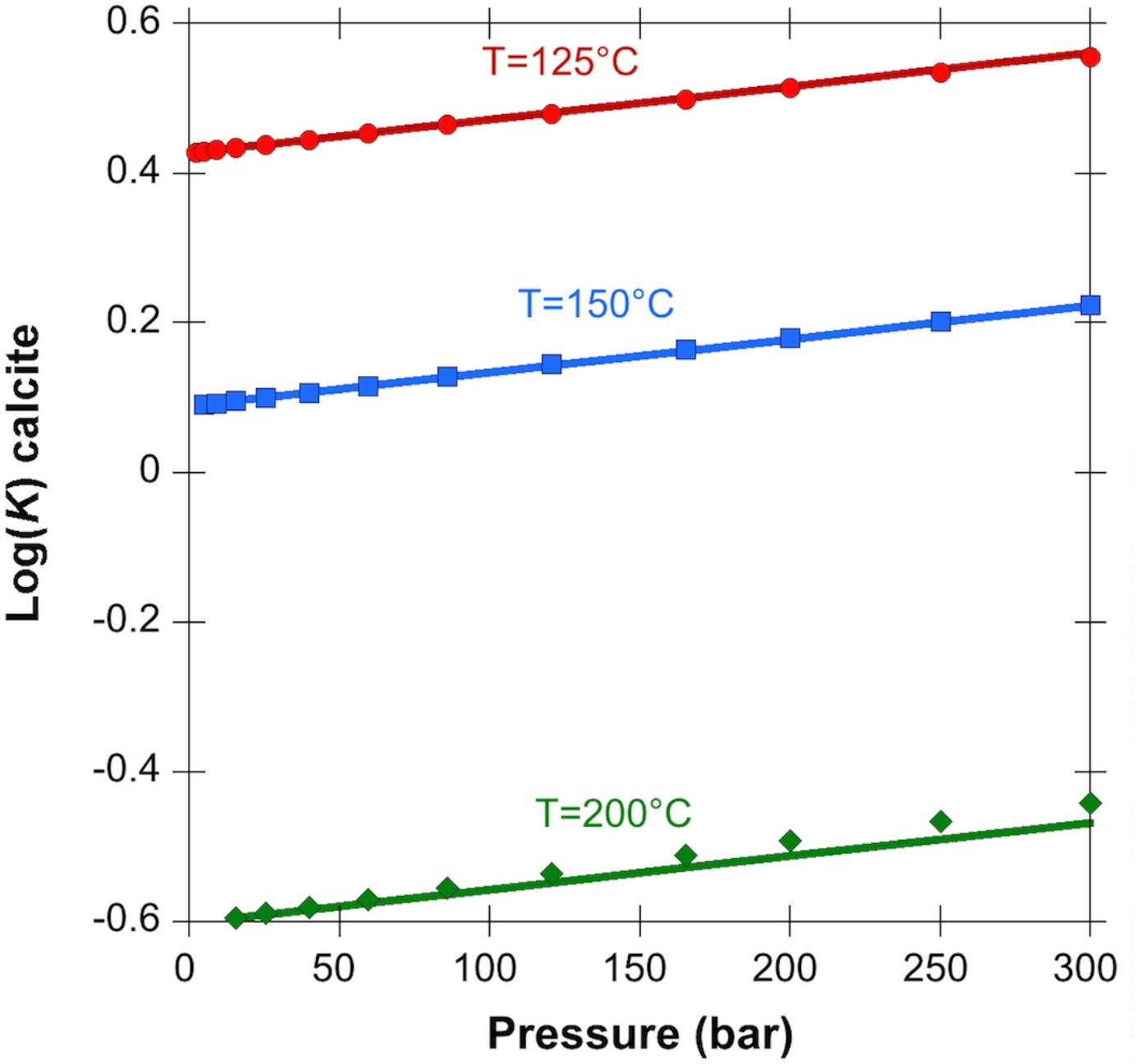
0.6
0.4
0.2
0
-0.2
-0.4
-0.6
0
50
100
150
200
250
300
T=125°C
T=150°C
T=200°C
Log(K) calcite
Pressure (bar)

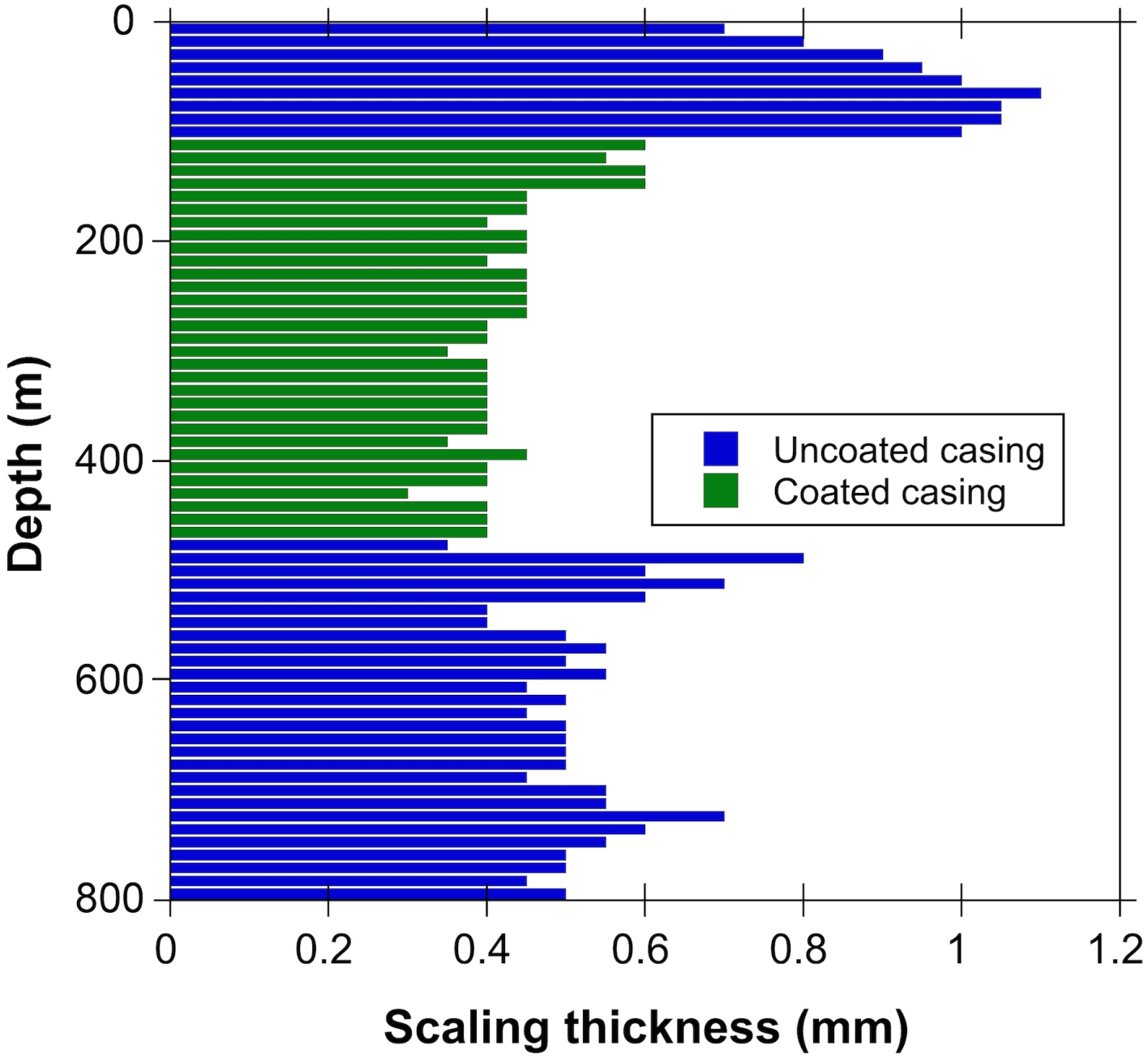
0
200
400
600
800
Depth (m)
0
0.2
0.4
0.6
0.8
1
1.2
Scaling thickness (mm)
Uncoated casing
Coated casing

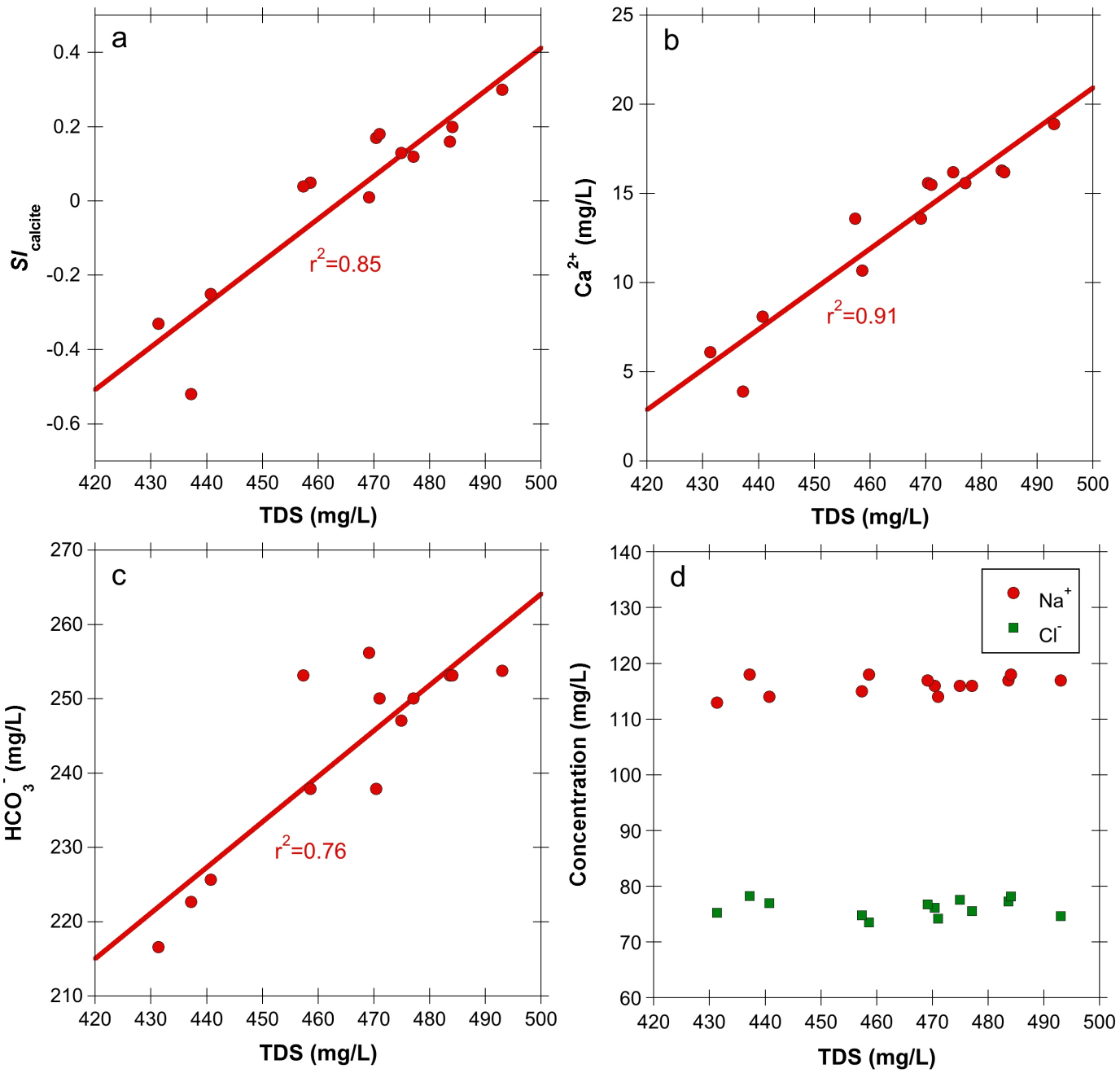
a
SI calcite
r2=0.85
TDS (mg/L)
b
Ca2+ (mg/L)
r2=0.91
TDS (mg/L)
c
HCO3- (mg/L)
r2=0.76
TDS (mg/L)
d
Na+
Cl-
Concentration (mg/L)
TDS (mg/L)

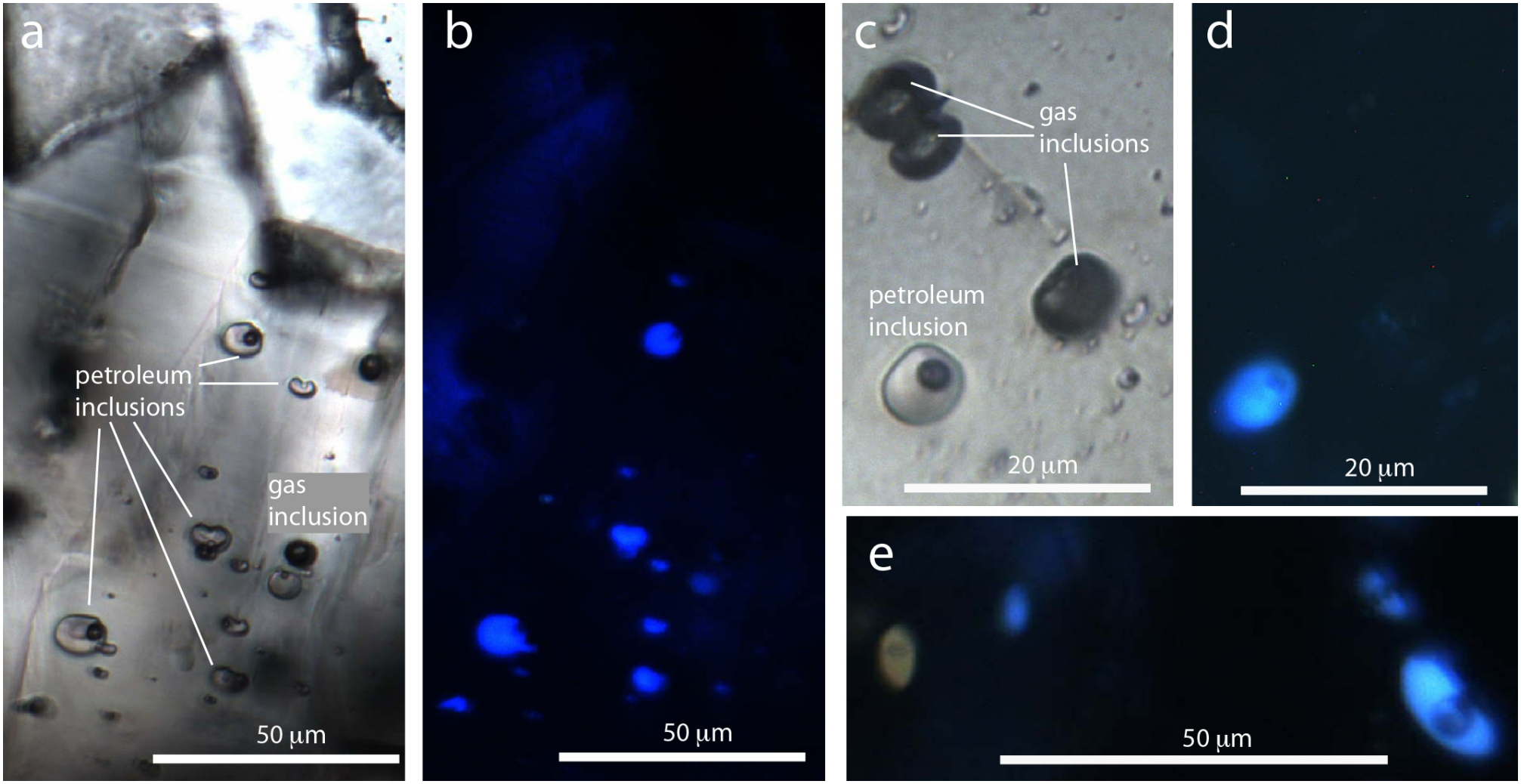
a
petroleum
inclusions
gas
inclusion
50 μm
b
50 μm
c
gas
inclusions
petroleum
inclusion
20 μm
d
20 μm
e
50 μm

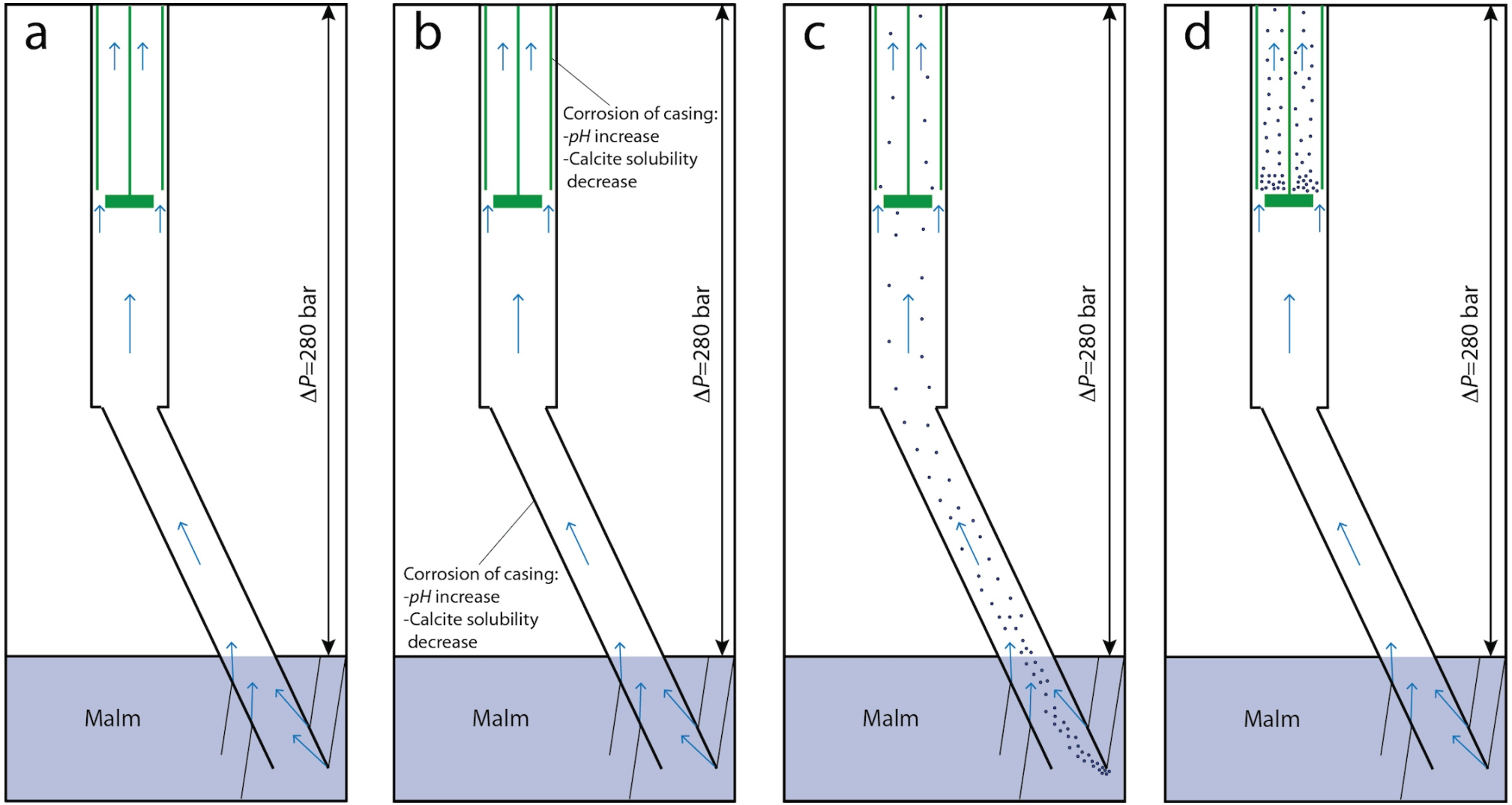
a
b
c
d
ΔP=280 bar
Malm
Corrosion of casing:
-pH increase
-Calcite solubility
decrease

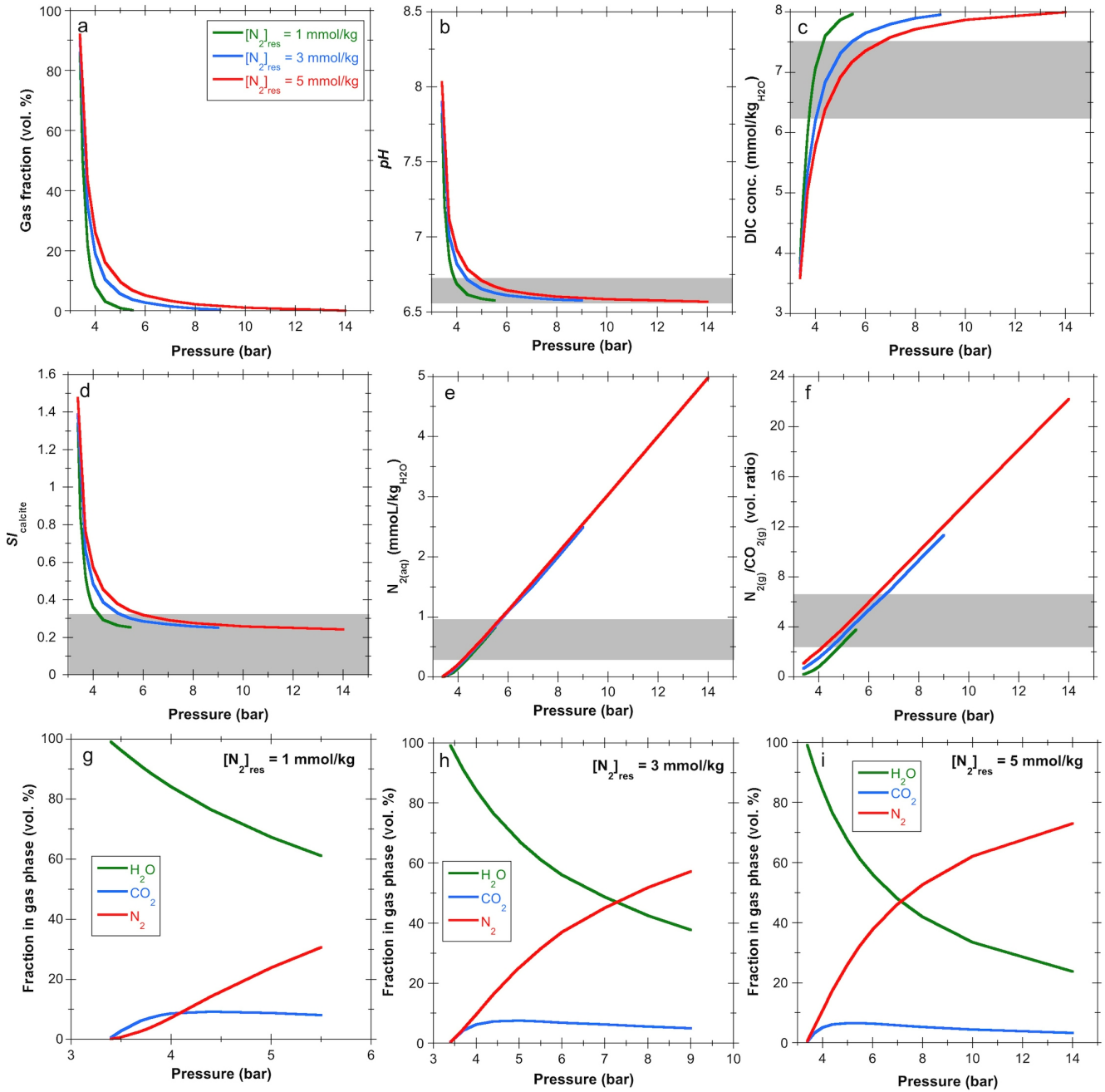
a
[N2]res = 1 mmol/kg
[N2]res = 3 mmol/kg
[N2]res = 5 mmol/kg
Gas fraction (vol. %)
Pressure (bar)
b
pH
Pressure (bar)
c
DIC conc. (mmol/kgH2O)
Pressure (bar)
d
SIcalcite
Pressure (bar)
e
N2(aq) (mmoL/kgH2O)
Pressure (bar)
f
N2(g)/CO2(g) (vol. ratio)
Pressure (bar)
g
[N2]res = 1 mmol/kg
H2O
CO2
N2
Fraction in gas phase (vol. %)
Pressure (bar)
h
[N2]res = 3 mmol/kg
H2O
CO2
N2
Fraction in gas phase (vol. %)
Pressure (bar)
i
[N2]res = 5 mmol/kg
H2O
CO2
N2
Fraction in gas phase (vol. %)
Pressure (bar)

Table 1: Mineralogical and chemical scaling composition observed at various locations within the production well

Location of scaling formation	Main mineral phase	Accessory mineral phases	Chemical composition[1]	
Pump	Calcite	Bornite (Cu_5FeS_4) Digenite (Cu_9S_5) Chalcopyrite ($CuFeS_2$)	Ca (wt %): $^2CO_3^{2-}$ (wt %): Mg (wt %): Fe (wt %): ^3S (wt %): K (wt %): Cu (wt %): Na (wt %): Mg/Ca: (mol ratio)	36.9 ± 0.2 59.6 ± 0.6 1.66 ± 0.12 0.97± 0.48 0.76 ± 0.45 0.02 ± 0.01 0.10 ± 0.02 0.03 ± 0.01 0.07
Uncoated casing	Calcite	Magnetite (Fe_3O_4) Pyrrhotite (FeS) Pyrite (FeS_2)	Ca (wt %): $^2CO_3^{2-}$ (wt %): Mg (wt %): Fe (wt %): ^3S (wt %): K (wt %): Cu (wt %): Na (wt %): Mg/Ca: (mol ratio)	37.2 ± 0.3 59.2 ± 0.4 1.32 ± 0.21 1.87 ± 0.62 0.36 ± 0.19 0.05 ± 0.04 <0.01 <0.01 0.06
Coated casing	Calcite	-	Ca (wt %): $^2CO_3^{2-}$ (wt %): Mg (wt %): Fe (wt %): ^3S (wt %): K (wt %): Cu (wt %):. Na (wt %): Mg/Ca: (mol ratio)	37.8 ± 0.1 60.3 ± 0.2 1.46 ± 0.03 0.26 ± 0.19 0.07 ± 0.02 0.06 ± 0.05 <0.01 <0.01 0.06

[1]Average composition; full analyses are provided in the electronic appendix. Uncertainties refer to the standard deviation (1σ) derived from measurements of multiple samples.
[2]Calculated from Mg and Ca, since electron microprobe analyses of individual crystals show that all Mg and Ca is derived from Mg-bearing calcite
[3]Calculated from SO_4^{2-}

Table 2: Chemical analyses of wellhead samples collected during October 2014 and September 2015. Also shown are geochemical speciation calculations performed to reconstruct the composition under reservoir conditions as well as to simulate the linear decompression scenario.

			KST-1	KST-2	KST-3	KST-4	KST-5	KST-6	KST-7	KST-8	KST-9	KST-10	KST-11	KST-12	Reservoir recon-struction[1]	Linear P-drop scenario[1]	Linear P-drop + calcite prec.[1]
		Sampling date	16.10. 2014	13.01. 2015	03.02. 2015	03.03. 2015	31.03. 2015	28.04. 2015	26.06. 2015	10.07. 2015	10.09. 2015	15.09. 2015	17.09. 2015	24.09. 2015	n.a	n.a	n.a
in situ measurements	Production rate	L/s	91	89.9	87.8	82.2	84.4	76.4	106	128.5	120	120	130	130	n.a.	n.a.	n.a.
	Temperature	°C	135	134	134.0	134.4	133.8	135.6	134.2	135	135.1	135	135	135	140	135	135
	Pressure	bar	16.4	17.3	17.2	17.1	18	16	18	18	17	19	19	19	300	18	18
	Degassing pressure	bar	8	10	7	4	5	2	3	4	3.5	2.5	3.5	3.5	n.a.	n.a.	n.a.
	pH at 20 °C	-	6.26	6.35	6.29	6.37	6.35	6.42	6.42	6.36	6.38	6.27	6.40	6.30	n.a.	n.a.	n.a.
	pH (wellhead *P,T*)[1]	-	6.58	6.65	6.61	6.54	6.61	6.68	6.59	6.60	6.66	6.55	6.66	6.67	6.44	6.55	6.52
	Eh	mV	-109	-199	-114	-166	-132	-52	-105	-122	-81	-57	-89	-95	n.a.	n.a.	n.a.
	O_2	mg/l	< 0,1	< 0,1	< 0,1	< 0,1	< 0,1	< 0,1	< 0,1	<0,1	< 0,1	< 0,1	< 0,1	< 0,1	n.a.	n.a.	n.a.
water analysis	Na^+	mg/L	113	116	117	117	116	118	115	116	114	118	118	117	117	117	117
	K^+	mg/L	16.2	16.8	16.9	16.8	17.1	16.7	16.5	16.5	16.5	16.8	16.7	16.9	16.9	16.9	16.9
	Ca^{2+}	mg/L	6.1	15.6	16.3	13.6	15.6	10.7	13.6	16.2	15.5	3.9	16.2	18.9	18.9	18.9	13.7
	Mg^{2+}	mg/L	1.9	2.1	2.1	2	2	2	2	1.9	1.9	2.1	2	2	2	2	2
	[1]HCO_3^-	mg/kg	195	226	233	227	228	222	221	228	225	200	228	241	243	242	229
	[1]$CO_{2(aq)}$	mg/kg	133	126	142	164	141	120	145	146	126	144	128	132	173	174	179
	DIC	mmol/L	6.25	6.64	7.12	7.51	7.01	6.41	6.98	7.11	6.61	6.58	6.73	7.03	8.0	8.0	7.87
	Cl^-	mg/L	75.3	76.2	77.3	76.8	75.6	73.5	74.8	77.6	74.2	78.3	78.2	74.7	74.7	74.7	74.7
	F^-	mg/L	3.2	3.6	3.5	3.1	3.7	3.4	3.8	3.4	n.m.	3.8	4.0	3.8	3.8	3.8	3.8
	SO_4^{2-}	mg/L	6.1	6.7	6.1	5.4	7.1	7.9	6.2	5.8	5.9	6.3	6	5.7	5.7	5.7	5.7
	TDS	mg/L	431.4	470.7	483.7	469.1	477.1	458.6	457.3	474.9	471.0	437.2	484.1	493	487.7	487.5	468.3
	$HS^- + S^{2-}$	mg/L	6.14	8.2	5.8	7.4	7.3	6.7	n.m	n.m	7.48	8.1	8.1	7.8	7.8	7.8	7.8
	[4]DOC	mg/L	2	0.78	1.13	1.4	n.m	1.7	n.m	n.m	n.m	n.m	n.m	1.2	n.s.	n.s.	n.s.
	[5]$SI_{calcite}$	-	-0.33	0.17	0.16	0.02	0.12	0.05	0.04	0.13	0.18	-0.52	0.20	0.30	0.02	0.18	0.00
	$SI_{dolomite}$	-	-0.40	0.26	0.23	-0.02	0.15	0.17	0.05	0.13	0.26	-0.61	0.30	0.42	-0.07	0.24	-0.01
gas analysis[2]	H_2	mmol/kg	<0.01	0.01	0.01	0.01	0.01	<0.01	<0.01	0.01	<0.01	n.m.	n.m.	n.m.	n.s.	n.s.	n.s.
	Ar	mmol/kg	0.01	0.02	0.02	0.02	0.03	0.01	0.01	0.01	0.01	0.01	0.02	0.02	n.s.	n.s.	n.s.
	N_2 (124)[3]	mmol/kg	0.55	0.83	0.88	0.78	0.94	0.30	0.64	0.81	0.41	0.39	0.50	0.36	n.s.	n.s.	n.s.
	CO_2 (1370)[3]	mmol/kg	2.70	2.74	2.97	3.31	2.91	2.51	2.83	3.06	2.51	2.93	2.58	2.87	n.s.	n.s.	n.s.
	Methane (CH_4) (191)[3]	mmol/kg	1.02	1.71	1.76	1.65	1.84	0.83	1.12	1.54	1.01	0.99	1.24	1.04	n.s.	n.s.	n.s.
	H_2S	mmol/kg	0.19	0.26	0.18	0.23	n.m.	n.m.	n.m	n.m	n.m	n.m	n.m	n.m	n.s.	n.s.	n.s.
	Ethane (C_2H_6)	mmol/kg	0.01	0.03	0.02	0.02	0.03	0.01	0.02	0.02	0.01	0.01	0.02	0.01	n.s.	n.s.	n.s.
	Propane (C_3H_8)	mmol/kg	0.01	0.01	0.01	0.01	0.01	<0.01	0.01	0.01	n.m	n.m	n.m	<0.01	n.s.	n.s.	n.s.
	Butane (C_4H_{10})	mmol/kg	<0.01	0.01	0.01	0.00	0.01	<0.01	<0.01	0.01	<0.01	n.m	n.m	<0.01	n.s.	n.s.	n.s.
	Total gas content	mmol/kg	4.31	5.35	5.69	5.80	5.76	3.67	4.64	5.45	3.97	4.33	4.38	4.31	n.s.	n.s.	n.s.

[1]Obtained from geochemical modeling
[2]Concentrations refer to gases dissolved in wellhead samples
[3]Equilibrium concentration at reservoir *P,T* conditions (300 bar, 140°C) at the presence of a corresponding gas phase
[4]Dissolved organic carbon (DOC)
[5]Corresponds to the saturation index of the proposed solid solution ($Ca_{0.94}Mg_{0.06}CO_3$)
n.m.: not measured; n.s.: not simulated, n.a.: not applicable

Table 3: Chemical composition of gases liberated from liquid and gas inclusions during crushing of calcite scalings collected from various casing tubes along the production well.

[1]Gas		Casing #3 (z = -35 m)	Casing #7 (z = -82 m)	Casing #32 (z = -365 m)	Casing #60 (z = -694 m)
N_2	Vol %	73.6	70.1	87.4	82.4
CO_2	Vol %	25.5	29.6	12.6	16.8
CH_4	Vol %	0.60	0.23	0.31	0.2
N_2/CO_2	-	2.89	2.37	6.91	4.89
[2]Sum		99.7	99.8	99.9	99.5

[1]Composition normalized to 100%. Vapor (i.e, H_2O gas) was not determined and does not appear in the analyses. Differences to 100% correspond to hydrocarbon gases other than CH_4.

[2]Difference to 100% corresponds to minor amounts of methane, ethane, propane, butane, and pentane

Table 4: Comparison of wellhead fluid composition predicted from boiling calculations with that determined on the sample that is least affected by scaling formation (KST-12). Also shown is the simulated N_2/CO_2 ratio of the coexisting gas phase in comparison to the ratio measured in gas inclusions within calcite (Table 3).

		Liquid phase						Gas phase				
	P_{degas} (bar)	DIC (mmol/kg)	HCO_3^- (mg/kg)	CO_2 (mg/kg)	$N_{2(aq)}$ (mmol/kg)	pH	$SI_{calcite}$	Gas fraction (Vol %)	$[H_2O]$ (vol. %)	$[N_2]$ (vol. %)	$[CO_2]$ (vol. %)	$(N_2/CO_2)_{gas}$
[1]**Simulation**	4.6	7.03	241	132	0.44	6.69	0.35	8.4	73.20	19.35	7.45	2.60
[2]**KST-12**	-	7.03	241	132	0.36	6.67	0.30	-	-	-	-	2.37-6.9

- Unknown

[1]$[N_2]_{reservoir}$ = 3 mmol/kg

[2]Sample with max. $SI_{calcite}$ and [Ca] implying minimum amounts of scaling formation

- Extensive geochemical characterization of calcite scales and wellhead fluid samples
- Wellhead compositions reveal that the rate of scaling formation is highly variable
- Identification of gas inclusions demonstrates the presence of a free gas phase
- Geochemical modeling indicate a minimum pressure of 4-6 bar in the production well
- CO_2 exsolution upon boiling at the pump is a main driver for scaling formation

Fig. S1. Diffractogramms of scales collected from the pump (a), the coated (b), and the uncoated casing (c).

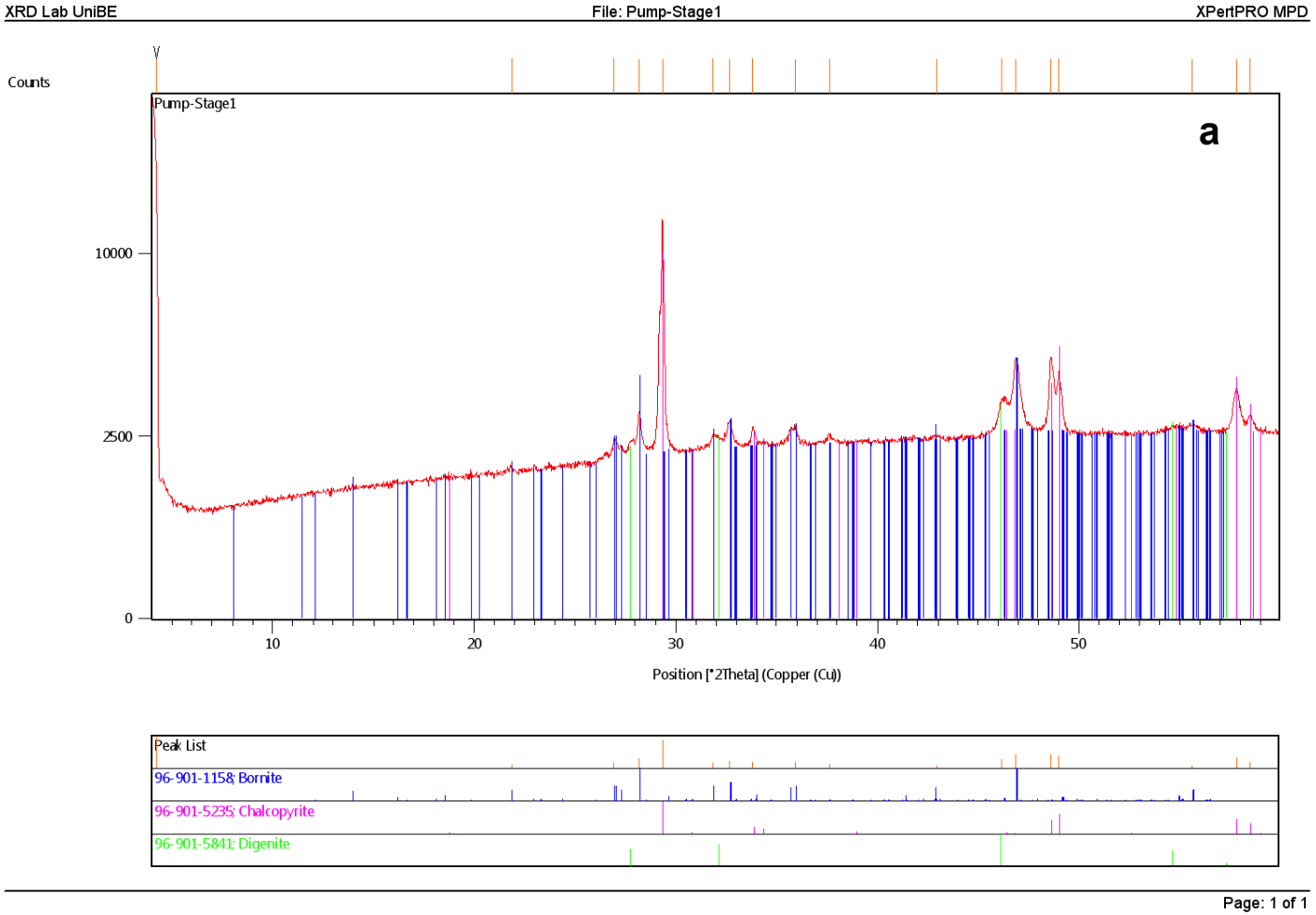

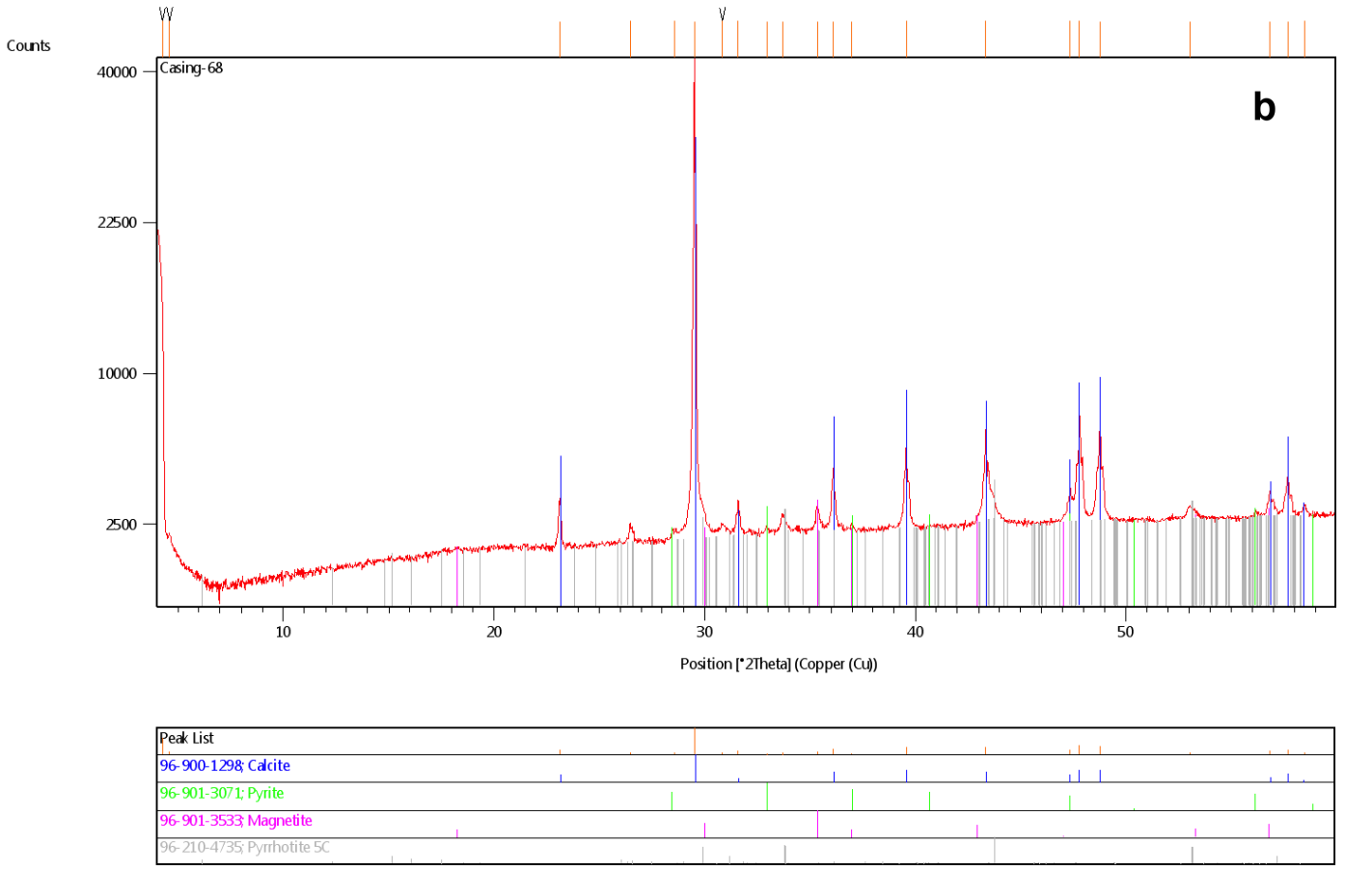
Counts
Casing-68
b
40000
22500
10000
2500
10
20
30
40
50
Position [°2Theta] (Copper (Cu))
Peak List
96-900-1298; Calcite
96-901-3071; Pyrite
96-901-3533; Magnetite
96-210-4735; Pyrrhotite 5C

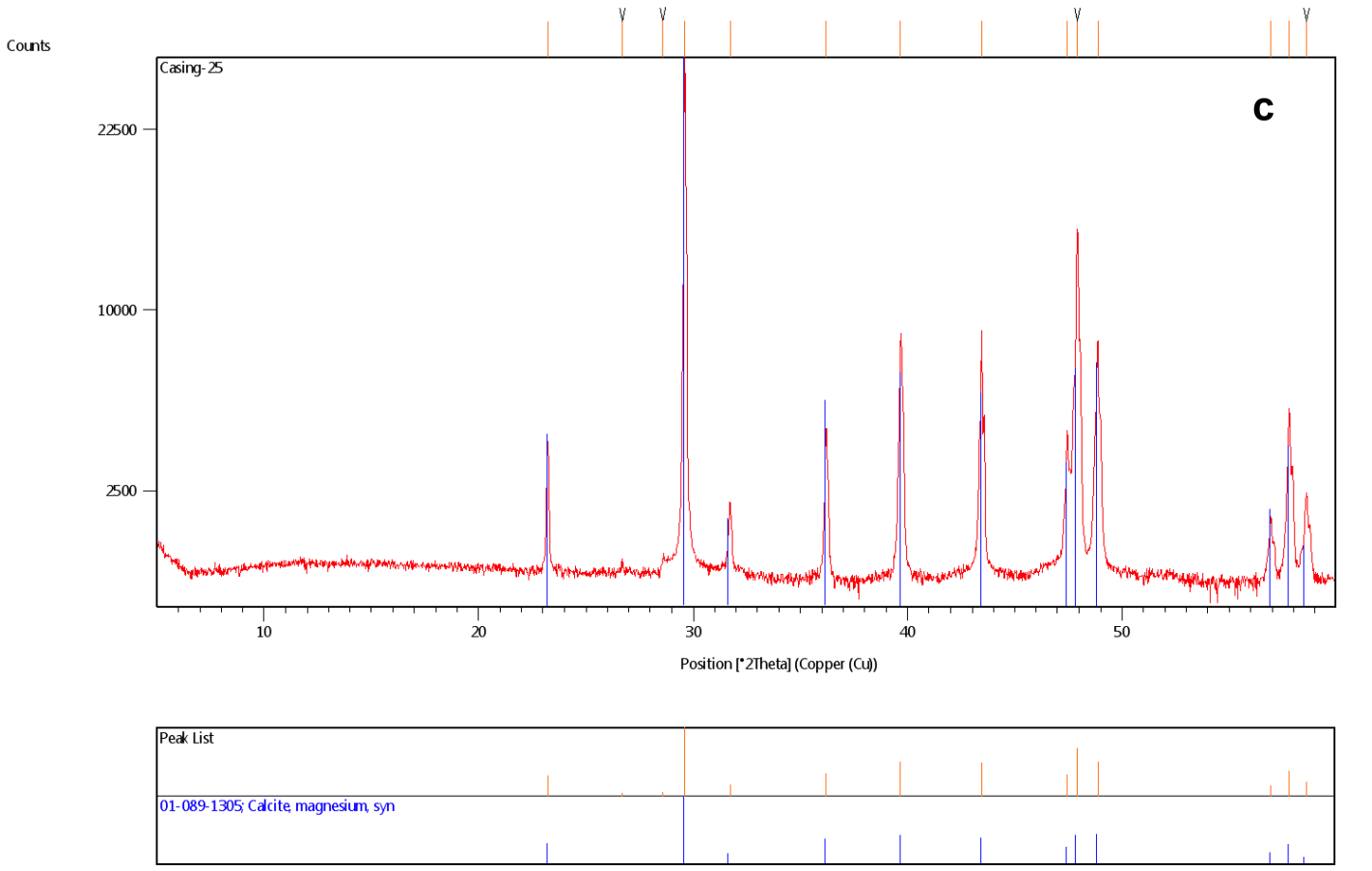
Counts
Casing-25
C
22500
10000
2500
10
20
30
40
50
Position [°2Theta] (Copper (Cu))
Peak List
01-089-1305; Calcite, magnesium, syn

Table S1: Production rates over the investigate production period from December 7, 2014 to March 15, 2015

Period	Produced fluid (m^3)	Average production rate (L/s)
07.12.-31.12.2014	189456	90.0
01.01.-31.01.2015	239031	89.8
01.02.-28.02.2015	205269	85.3
01.03.-15.03.2015	103083	80.1
Full period	736839	86.6

Table S2: Thermodynamic data of reactions relevant for performing geochemical speciation calculations of the investigated carbonate system

	Reaction type	Reaction stoichiometry	[1]log(K); T=125 °C, P=2.32 bar	[1]log(K); T=150°C, P=4.76 bar	Regression coefficients to calculate ΔV (eq. 2)
Calcite	Mineral reaction	$CaCO_3+H^+ = Ca^{2+} + HCO_3^-$	0.43	0.10	a_P=0.99 b_P=-0.084 c_P=0 d_P=0 e_P=0
Dolomite	Mineral reaction	$CaMg(CO_3)_2+2H^+ = Ca^{2+}+Mg^{2+}+2HCO_3^-$	0.37	-0.44	a_P=0.01 b_P=-0.165 c_P=0 d_P=0 e_P=0
$CO_{2(aq)}$	Aqueous complexation	$CO_{2(aq)}+H_2O = H^++ HCO_3^-$	-6.53	-6.72	a_P=0.001 b_P=-0.099 c_P=0 d_P=0 e_P=0
OH^-	Aqueous complexation	$OH^-+ H^+ = H_2O$	11.90	11.63	a_P=0.001 b_P=0.03 c_P=0.00009 d_P=0.1 e_P=0
$CO_{2(g)}$	Gas equilibrium	$CO_{2(g)}+H_2O = H^++ HCO_3^-$	-8.56	-8.77	a_P=0.001 b_P=0.006 c_P=0.0000008 d_P=0 e_P=0

[1]Equilibrium constants log(*K*) were defined according to the Soltherm.H06 database (Reed and Palandri, 2006). The temperature dependence is calculated according to $\log(K)_{T[K]}=a_T*\ln(T_K) + b_T + c_T*T_K* d_T/T_K + e_T/T_K^2$, where a_T, b_T, cT, d_T and e_T are constants defined in the database. For the listed mineral phases, however, the interpolation between T=125°C and T=150°C is almost linear.

Table S3: Chemical composition of selected scaling samples

Sample	Type	Na (wt %)	K (wt %)	Mg (wt %)	Ca (wt %)	[1]CO_3^{2-} (wt%)	[2]S (wt%)	Fe (wt%)	Cu (wt %)	Mg/Ca (mol ratio)
Casing 1	uncoated	0.01	0.09	0.91	37.49	58.50	0.42	2.58	<0.01	0.04
Casing 7	uncoated	<0.01	0.10	1.45	36.91	58.97	0.14	2.42	<0.01	0.06
Casing 9	uncoated	<0.01	0.02	1.45	36.95	59.12	0.20	2.26	<0.01	0.06
Casing 10	coated	0.02	0.09	1.49	37.63	60.13	0.10	0.54	<0.01	0.07
Casing 25	coated	<0.01	0.01	1.49	37.83	60.47	0.05	0.15	<0.01	0.06
Casing 40	coated	<0.01	0.12	1.43	37.86	60.36	0.06	0.18	<0.01	0.06
Casing 41	coated	<0.01	0.03	1.45	37.87	60.41	0.06	0.18	<0.01	0.06
Casing 44	uncoated	<0.01	0.02	1.40	37.26	59.38	0.48	1.48	<0.01	0.06
Casing 56	uncoated	0.01	0.03	1.40	37.41	59.62	0.28	1.24	<0.01	0.06
Casing 68	uncoated	0.01	0.05	1.30	37.40	59.37	0.65	1.22	<0.01	0.06
Pump intake	pump	0.02	0.01	1.74	37.03	60.01	0.44	0.64	0.11	0.08
Pump stage 1	pump	0.03	0.02	1.57	36.79	59.11	1.07	1.31	0.09	0.07

[1]calculated from Mg and Ca assuming that all Mg and Ca is derived from Mg-bearing calcite
[2]calculated from SO_4^2